CHAPTER 4

Results and Discussion

4.1 Chemical Analysis and Phase Identification of Base ASSs

Chemical analysis by glow discharge spectrometry (GDS) is summarized in Table 4.1, as compared to classification range of ASSs given in Table 4.2. The results in Table 4.1 indicated that chemical composition of the as-received base ASSs fell within the classification range. The AISI 304L contains higher carbon content than that mentioned in the standard range. In cases of modified 201 ASSs (201-1M and 201-2M), their compositions can be classified as AISI 201 based on their manganese contents. However, their copper content is close to that of AISI 204Cu. The chromium content of the AISI 202 was found to be lower than that mentioned in the standard range. Sulfur content in 201-1M is higher than that in other steels. Therefore, resistance to pitting corrosion of 201-1M may be inferior to that of other steels, because sulfur can react with chromium and manganese enhancing Cr-depleted zones around sulphide inclusions as suggested by Pardo *et al*. (2008).

Composition analysis, as Cr- and Ni-equivalent numbers, was performed using the following equations (after Blondeu (2008)):

$$Cr_{eq} = Cr + 1.37Mo + 1.5Si + 2Nb + 3Ti \quad (4.1)$$

$$Ni_{eq} = Ni + 0.31Mn + 22C + 14.2N + Cu \quad (4.2)$$

and given in Table 4.3. Prediction plots on the Schäffler-Bystram diagram are given in Figure 4.1.

Table 4.1 Chemical Analysis of Base ASSs by GDS

Element (wt%)	**AISI 304**	**AISI 304L**	**201-1M**	**201-2M**	**AISI 202**
C	0.0603	0.0412	0.0805	0.0930	0.0553
Si	0.4849	0.4071	0.8524	0.5915	0.4424
Mn	1.1107	1.3713	4.8933	5.6360	7.0660
P	0.0263	0.0239	0.0357	0.0381	0.0511
S	0.0031	0.0060	0.0116	0.0029	0.0024
Cr	18.4667	18.1000	17.067	17.7067	14.8400
Ni	8.9887	8.9187	4.1393	2.1733	4.6433
Mo	0.1071	0.0847	0.1099	0.1193	0.1598
Cu	0.1937	0.1429	2.5027	2.1900	1.5793
Ti	0.0203	0.0064	0.0181	0.0056	0.0057
Nb	0.0031	0.0069	0.0817	0.0640	0.0020
N	0.0330	0.0590	0.4300	0.2386	0.0562
Fe	Bal.	Bal.	Bal.	Bal.	Bal.

Table 4.2 UNS Chemical Composition of ASSs

Element (wt%)	**AISI 304** S 30400	**AISI 304L** S 30403	**AISI 201** S 20100	**AISI 202** S 20200	**AISI 204Cu** S 20400
C	0.05	0.02	0.08	0.48	0.15
Si	0.45	0.45	0.45	0.40	1.00
Mn	1.80	1.80	7.10	7.40	9.00
P	0.03	0.03	0.03	0.027	0.06
S	0.001	0.0013	0.001	0.001	0.03
Cr	18.30	18.30	16.30	16.10	17.0
Ni	8.10	8.10	4.50	4.04	3.00
Mo	0.30	0.30	0.20	0.194	1.00
Cu	0.30	0.40	**0.20**	1.64	**4.00**
Ti	N/A	N/A	N/A	N/A	N/A
Nb	N/A	N/A	N/A	N/A	N/A
N	0.05	0.09	0.07	0.106	0.30
Fe	Bal.	Bal.	Bal.	Bal.	Bal.

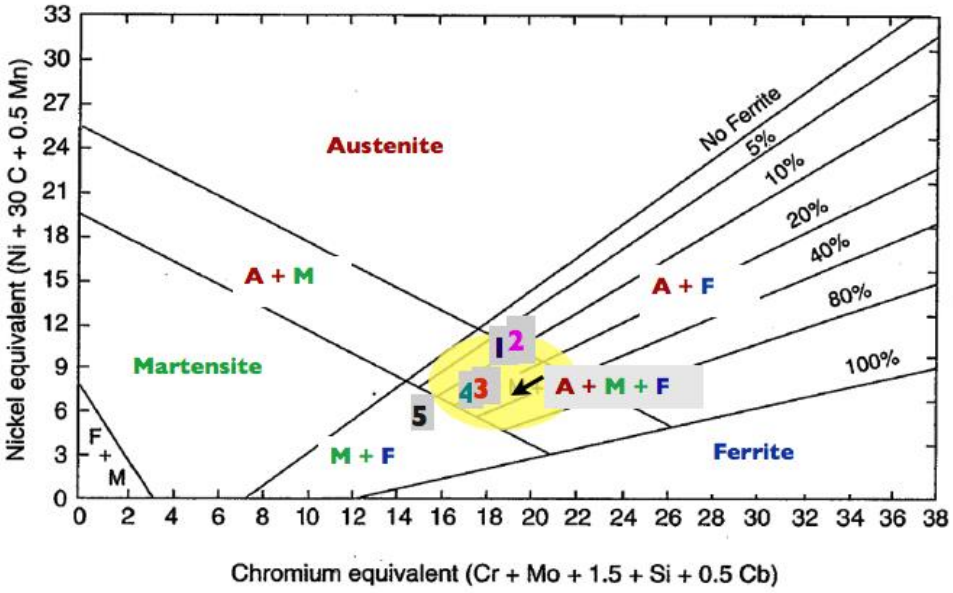

Figure 4.1Prediction plots in the Schäfler diagram from the chemical composition of base ASSs: (1) AISI 304, (2) AISI 304L, (3) 201-1M, (4) 201-2M and (5) AISI 202, respectively.

Table 4.3Calculated Parameters of Base ASSs

Calculations	**AISI 304**	**AISI 304L**	**201-1M**	**201-2M**	**AISI 202**
Cr_{eq}	19.3906	18.8463	19.3360	18.8833	15.7179
Ni_{eq}	11.3206	11.2318	16.0358	11.5453	10.4278
Cr_{eq}/Ni_{eq}	1.7129	1.6779	1.2058	1.6356	1.5073
$SFE(mJ/m^2)$	27.8842	27.4298	9.2870	8.1073	18.3944

The modified Schäfler diagram in Figure 4.1 indicates that main phases to be found in five ASSs in the present work should be austenite, martensite and ferrite. The amount of the austenite phase should be higher in the case of AISI 304 and AISI 304L with lower proportions of ferrite and martensite phases. The results from XRD spectra as shown in Figure 4.2 are in accord with the prediction in Figure 4.1. Base ASSs employed in the present work have been fabricated into a roll of sheet by cold-rolling process. The previous works by Padilha *et al*. (2003) and Talonen and Hänninen (2007) has discussed the effects of plastic deformation i.e. that cold-rolling possibly induces the martensitic transformation in austenitic stainless steels as $\gamma \rightarrow \varepsilon \rightarrow \alpha'$.. Therefore, the presence of martensite is expected to be induced by the applied cold-work.

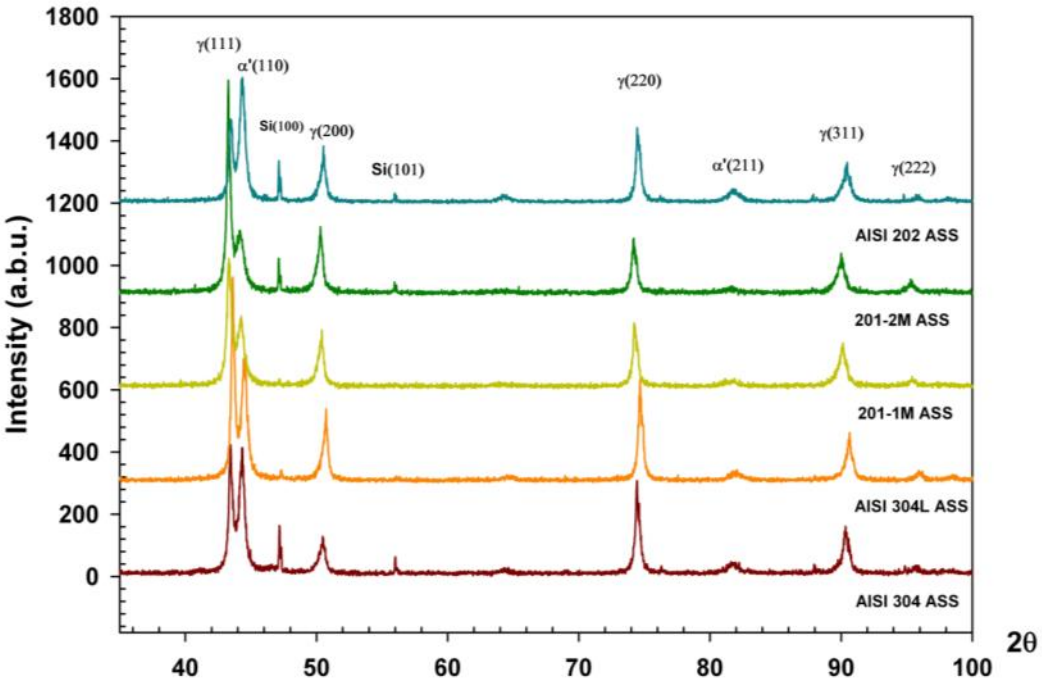

Figure 4.2Phase identification by XRD of base ASSs

(Peaks of Si_{100} and Si_{101} are from NIST SRM 640c standard intended as internal standard for peak-position correction.)

Stacking-fault energy (SFE) as predicted by the equation after Rondelli *et al.* (1995) as:

$$SFE = -53 + 6.2Ni + 0.7Cr + 3.2Mn + 9.3Mo \quad (4.3)$$

is also given in Table 4.3. Estimated values of SFE for AISI 304 and AISI 304L ASSs are higher than those for 201 and AISI 202 ASSs by around two to three times. Effects of manganese addition rendered the reduction in stacking fault energy as suggested by Lee and Choi (2000). In Fe-Mn binary alloy system with less than 13 wt% of Mn, SFE decreasing can be due to combine effects from increasing of austenite grain size and carbon content.

4.2 Pitting Corrosion Resistance of Base ASSs

Calculation of pitting corrosion resistance number (PREN) in the present work has followed $PREN_{Mn}$ formula (Eq. 2.8) suggested by Rondelli *et al*. (2005) and chemical analysis given inTable 4.1.The ASSs were tested for pitting corrosion resistance in 3.5 wt% NaCl electrolyte under deaerated environment by cyclic potentiodynamic polarization techniques. Morphology of pits observed in AISI 304 and 201-2M is given for example in Fig.4.3.

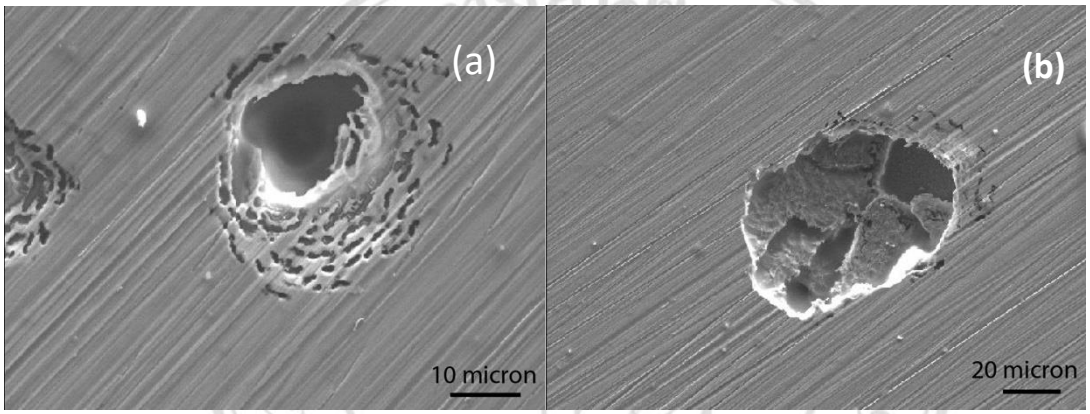

Figure 4.3 Morphology of pits in
(a) AISI 304 and (b) 201-2M after performed pitting resistance corrosion test by means of cyclic potentiodynamic polarization technique (secondary electron image in SEM)

$PREN_{Mn}$ calculation for base ASSs is given in Table 4.4, suggesting pitting corrosion resistance from high to low as: 201-1M > 201-2M > AISI 304L > AISI 304 > AISI 202. However, prediction by means of $PREN_{Mn}$ alone was not possible to explain the pitting corrosion resistance behavior. Average pit depths among ASSs were also summarized in Table 4.4, indicating higher pitting corrosion resistance in AISI 304 and AISI 304L. The amount of carbon content in AISI 304L was found higher than that was recommended in standard, whereas the amount of chromium content of AISI 202 was found lower - possibly weakening pitting corrosion resistance. Furthermore, higher contents of nitrogen and copper that had been added in 200 series may not be enough to withstand pitting corrosion as those in300 series - the results are in agreement to previous works by Olefjord and Wegrelius (1996) and Perez (2004). Consequently, the

as-received AISI 202 exhibited the highest susceptibility to pitting corrosion with deepest average pit depth among the as-received ASSs.

Table 4.4 $PREN_{Mn}$ and Pit Depth in Base ASSs

Base ASSs	$\boldsymbol{PREN_{Mn}}$	$\boldsymbol{SFE}$	**Pit Depth (micron)**
AISI 304	18.70	27.884	13.550 ± 2.268
AISI 304L	18.78	27.430	12.493 ± 2.866
201-1M	19.64	9.287	17.104 ± 0.892
201-2M	19.62	8.107	16.130 ± 0.393
AISI 202	9.99	6.677	18.997 ± 1.583

Effects of stacking fault energy (SFE), as previously given in Table 4.3 and here again in Table 4.4, are also important. Corrosion attack can normally occur along martensite and ferrite, but not austenite. Lower SFE steels may have greater susceptibility to combined damaging from stress corrosion cracking (SCC) due to an increase in martensitic transformation as suggested by Pardo *et al*. (2007). It had also been mentioned by de Abreu *et al*. (2007) that pitting corrosion starts at martensite. Hence, in higher SFE steels, higher slip resistance is expected to inhibit martensitic transformation.

The lower content of Ni by partially substitution of Mn in the Mn subsititution ASSs could have delayed healing process during repassivation and hence an increase in pit depth was found in the as-received 200 series. Not only the influence of major alloying elements such as Cr, Ni or Mn, the minor elements such as N, Cu, Ti, Si, S, and Sb also have their roles as either austenite or ferrite promoters in stainless steels composition. Moreover, cold-roll process can increase the amount of ferrite content in the ASSs and hence decrease their corrosion resistance.

Cyclic potentiodynamic polarization curves of base ASSsare shown in Fig. 4.4 and corrosion parameters are summarized in Table 4.5. It should be noted that corrosion potential (E_{corr}) and corrosion current density (I_{corr}) have been automatically obtained from Tafel plot analysis by Autolab GPES software (Appendix 2). Pitting potential (E_P) and repassivation potential (E_{rp}) have been located from polarization curves.

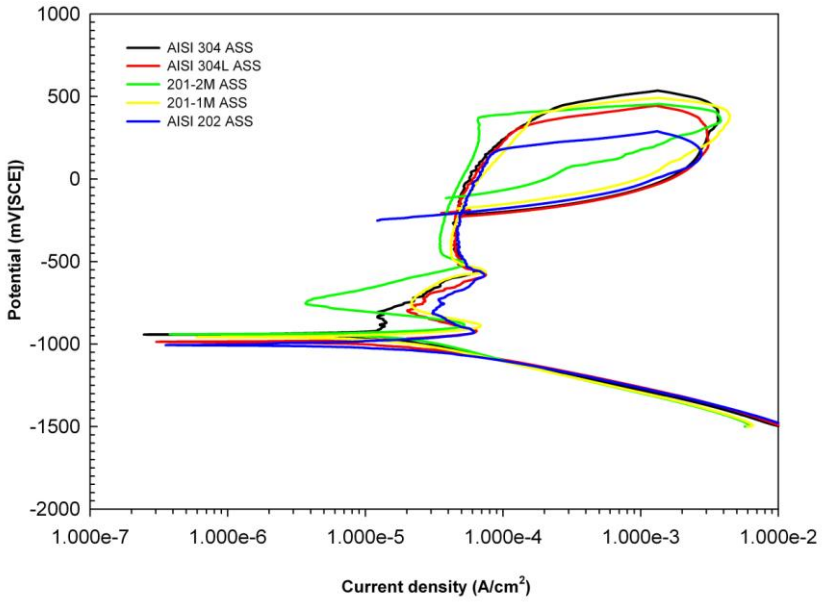

Figure 4.4 Cyclic potentiodynamic polarization curves of base ASSs

From cyclic potentiodynamic polarization curves, corrosion potential of AISI 304, 201-1M and 201-2M is seemingly similar. E_{corr} was defined by the point of intersection of the passive range of steel anodic curve with the active range of oxygen reduction reaction ($O_2 + 2H_2O + 4e^- \rightarrow 4OH^-$). AISI 304, 201-1M and 201-2M had E_{corr} fell almost within the same range, while E_{corr} of AISI 304L was a bit lower and of AISI 202 was the lowest. A decrease in E_{corr} means less time is needed for a formation of passive film (Alonso-Falleiros and Wolynec, 2002), hence formation of passive film was fastest for the case of AISI 202. This may result from less amount of chromium and copper together with higher amount of manganese and nitrogen as compared to those of AISI 304. Negative shifting for AISI 304L was possibly resulted from the higher carbon content from the recommended standard lowering its corrosion resistance.

The width of passivation range (E_p-E_{corr}) of 201-2M is comparable to that of AISI 304, which is the widest. AISI 202 possesses the narrowest passivation range and its pitting potential (E_p) was the lowest, so film breakdown or pitting of AISI 202 occurred at the earliest, possibly because of its comparatively low SFE. However, if (E_p-E_{rp}) is considered, those of AISI 202 and 201-2M are narrower as compared to others. This determines that the rate of repassivation in AISI 202 and 201-2M is comparatively fast, whereas that of 201-1M and AISI 304L is moderate and of AISI 304 is slow.

Figure 4.5 shows a trend between corrosion potential (E_{corr}) and pitting potential (E_p) of base ASSs. Among base ASSs, AISI 304, 201-1M and 201-2M have relatively high E_{corr} and E_p.

Table 4.5 Corrosion Parameters of Base ASSs

Base ASSs	E_{corr} (mV VS SCE)	I_{corr} ($\mu A/cm^2$)	E_p (mV VS SCE)	E_{rp} (mV VS SCE)	E_p-E_{corr} (mV)	E_p-E_{rp} (mV)	Note
AISI 304	-947 ± 13	4.95 ± 0.69	421 ± 8	-200	1368	621	Low corrosion current, wide passivation range and slow breakdown, but slow repassivation
AISI 304L	-970 ± 18	6.87 ± 1.39	342 ± 3	-200	1312	542	Faster passivation and repassivation, but higher corrosion current as compared to AISI 304
201-1M	-942 ± 16	8.33 ± 1.97	376 ± 19	-200	1318	576	Highest corrosion current and moderate passivation and repassivation
201-2M	-944 ± 3	7.74 ± 0.92	396 ± 27	-100	1340	496	Slower passivation and repassivation, but wider passivation range as compared to AISI 202
AISI 202	-1004 ± 4	5.92 ± 0.561	212 ± 9	-200	1216	412	Fast passivation and repassivation, but narrow passivation range and low pitting potential

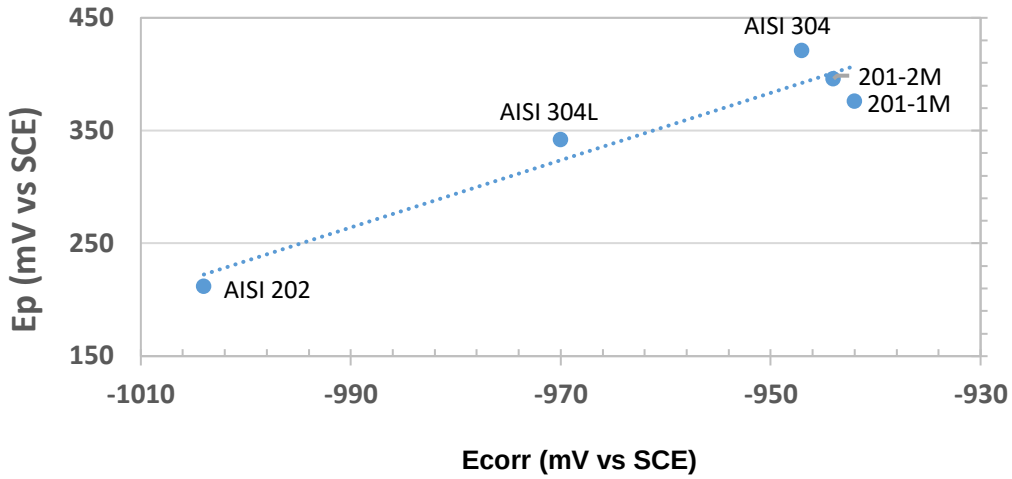

Figure 4.5 A trend between corrosion potential (E_{corr}) and pitting potential (E_p) of base ASSs

4.3 Intergranular Corrosion Susceptibility of Base ASSs

Higher DOS or *Pa* indicate higher susceptibility to the intergranular corrosion attack. Results from DOS test of base ASSs under deaerated condition are summarized in Table 4.6. It has indicated (Sidhom *et al*., 2007) that tested specimens are sensitized if the ratio of $I_r/I_a > 0.01$ and $P_a \gg 0$. Some of DL-EPR loops and morphology of ASSs prior and after DOS test are shown in Figures 4.6 to 4.8

Table 4.6 DOS Test of Base ASSs

Base ASSs	**Avg I_r (A/cm^2)**	**Avg I_a (A/cm^2)**	**Avg DOS**	**Avg *Pa* (C/cm^2)**
AISI 304	0.0085	0.0221	0.460 ± 0.123	4.777 ± 1.2796 (G = 16.94)
AISI 304L	0.002	0.003	0.607 ± 0.007	8.155 ± 1.002 (G = 13.09)
201-1M	0.008	0.015	0.553 ± 0.011	7.422 ± 0.148 (G = 13.12)
201-2M	0.007	0.013	0.533 ± 0.067	7.587 ± 0.956 (G = 15.80)
AISI 202	0.025	0.0191	0.762 ± 0.045	9.996 ± 0.585 (G = 13.42)

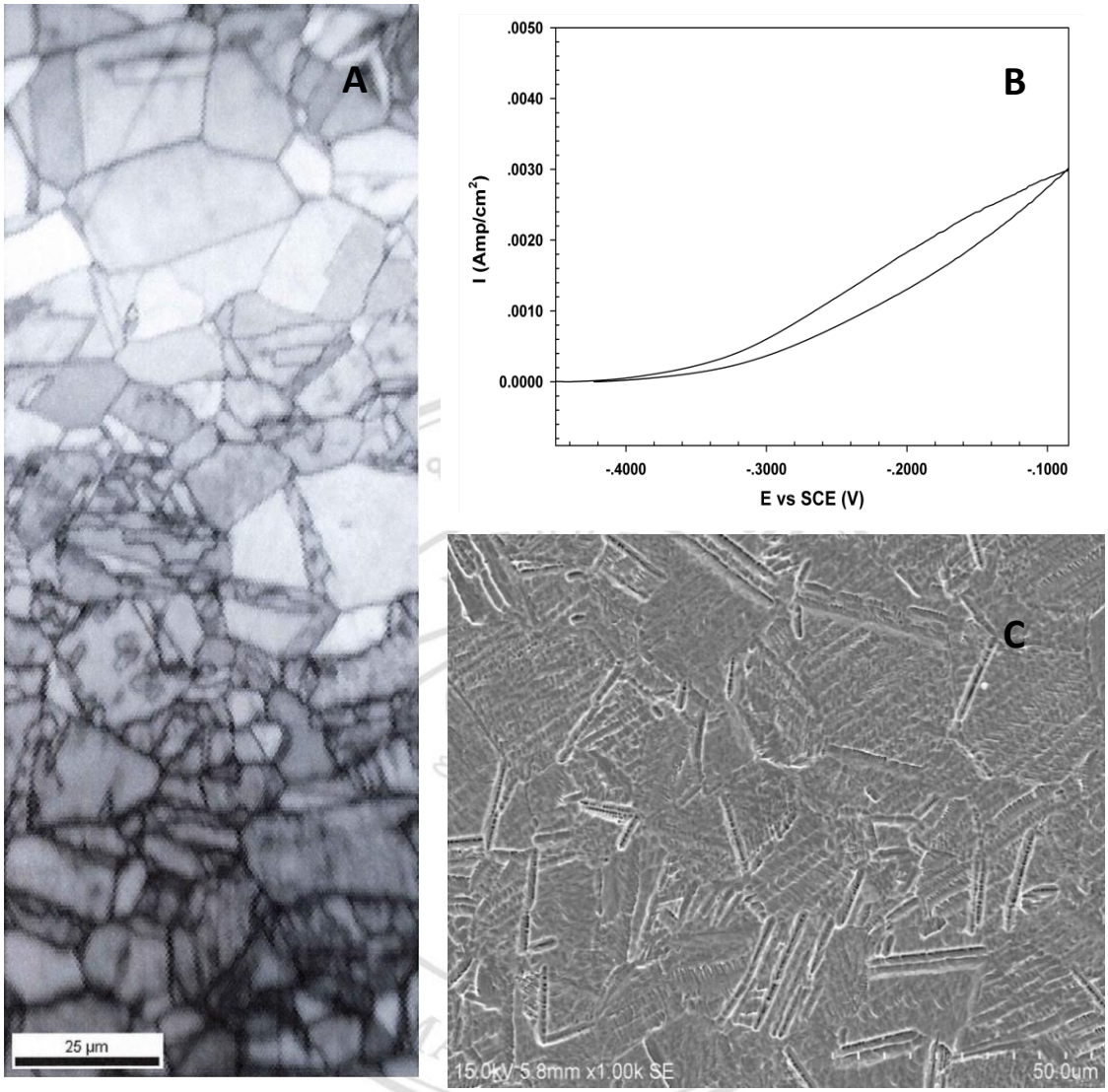

Figure 4.6 DOS test results of AISI 304 austenitic stainless steel:

(a) microstructure of original grain orientation in the normal direction to the cold-rolling direction (G = 16.94), (b) DL-EPR curve and (c) sensitized microstructure.

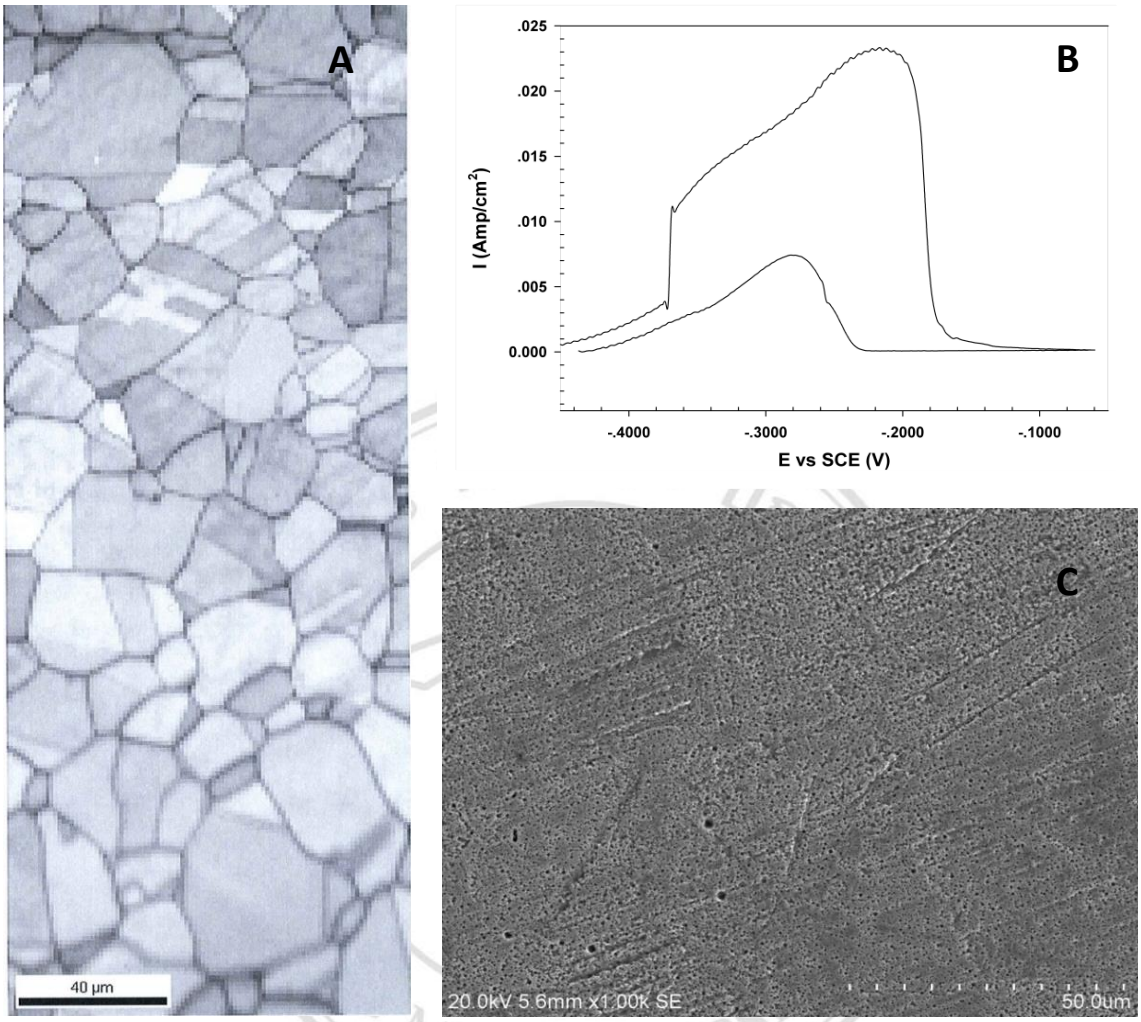

Figure 4.7 DOS test results of 201-2M austenitic stainless steel:

(a) microstructure of original grain orientation in the normal direction to the cold-rolling direction (G = 13.12), (b) DL-EPR curve and (c) sensitized microstructure.

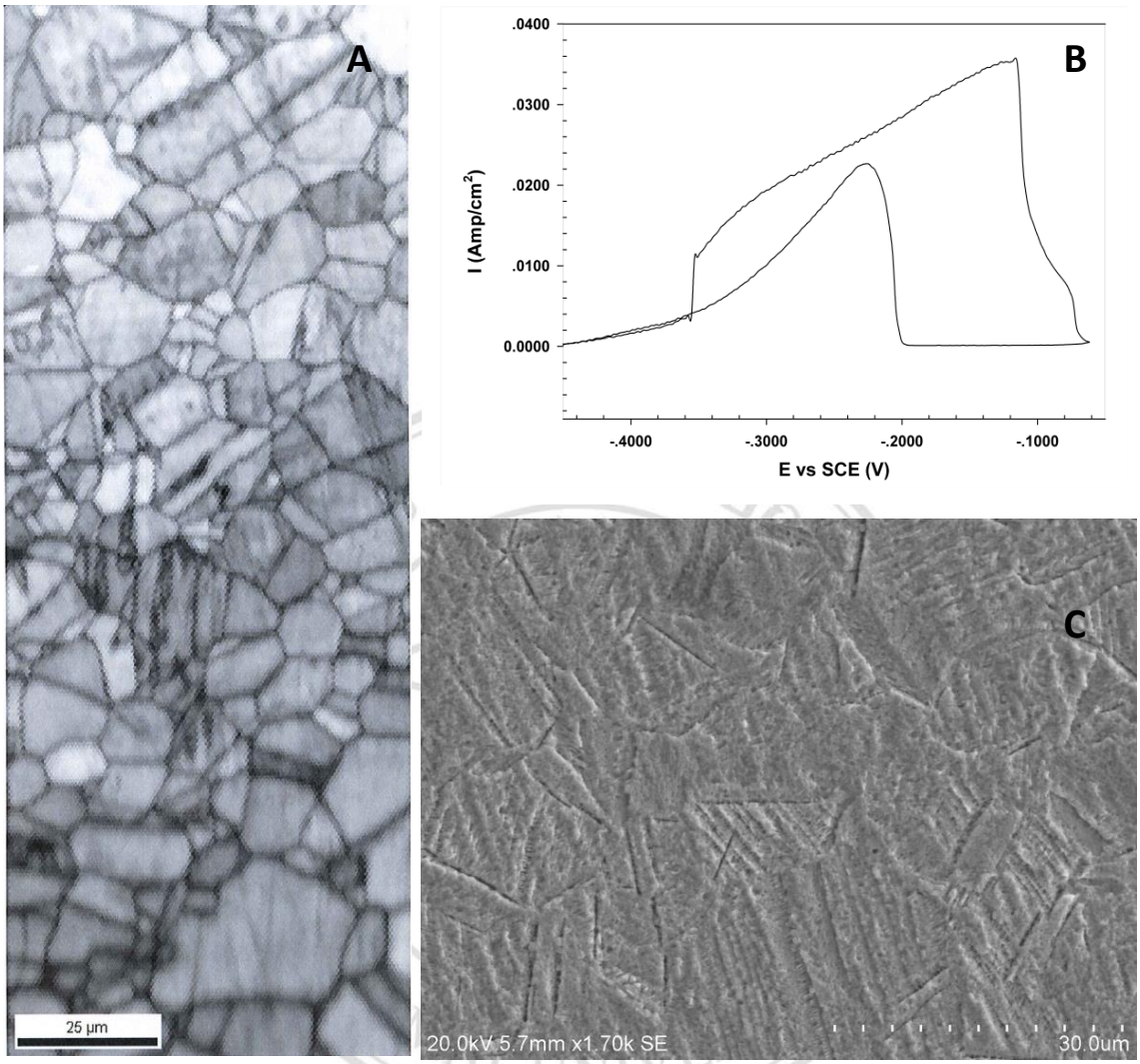

Figure 4.8 DOS test results of AISI 202austenitic stainless steel:

(a) microstructure of original grain orientation in the normal direction to the cold-rolling direction (G = 13.42), (b) DL-EPR curve and (c) sensitized microstructure.

In general, smaller grain size has more prone to intergranular corrosion. Trend of G value in Table 4.6 is in agreement with both DOS and *Pa*. G value of AISI 304 is the highest, its DOS and Pa are the lowest, and its sensitized microstructure can be classified as “step”. Regarding a decrease in IGC resistance of AISI 304L, the possible influence may derive from its higher carbon content.

G value of 201-2M is slightly higher than that of AISI 304. Even though its DOS is not much different to that of AISI 304, but its average Pa is almost double. The sensitized grain morphology should be classified as “dual” structure. Carbon, molybdenum, nitrogen and copper in proper proportion were added into modified 201 ASSs as to avoid precipitation of hardening phases, such as MC carbide that lead to an increase in susceptibility to grain boundary attack (Lo *et al*., 2009; Du Toit and Styn, 2012 and Freire *et al*., 2008). This is a possible explanation why some of modified 201 ASSs can exhibit DOS at comparable level to that of AISI 304.

Comparison between of grain morphology of AISI 202 before and after sensitization test showed severe corrosion attack at grain boundaries and exposed area to the electrolyte. Regardless of its lower grain number as compared to AISI 304L and 201-1M, deficient amount in chromium content may possibly the main cause of severe damage. Grain morphology after severe IGC attack to AISI 202 should be classified as “ditch” type.

The average DOS values of AISI 304, AISI 304L, 201-1M and 201-2M austenitic stainless steels are in a comparable range and in agreement with the results from average normalized charge calculation (*Pa*). AISI 202 austenitic stainless steel exhibited the highest susceptibility to IGC. The results are in agreement with those reported by Kiraa *et al*. (2007). 201-2M showed good IGC resistance potential to be used as an alternative to AISI 304. However, small addition of austenite promoter to 201-2M is still needs to improve its corrosion resistance. Nitrogen is one of possible additive elements as it is not expensive in gas form, particularly in the shielding gas during the welding.

4.4 Mechanical Properties of Base ASSs

4.4.1 Tensile Properties

Mechanical testing was carried out on base ASSs. Steel sheets were wired cut into dog bone shape for testing. The results of tensile stress and strain are summarized in Table 4.7.

Table 4.7 Tensile Properties of Base ASSs

Tensile stress (MPa)			
AISI 304	AISI 304L	201-2M	AISI 202
712.90 ± 2.21	684.04 ± 3.96	796.32 ± 1.63	739.96 ± 2.46
Tensile strain (%)			
AISI 304	AISI 304L	201-2M	AISI 202
57.13 ± 0.29	59.47 ± 0.14	50.30 ± 0.23	55.91 ± 0.33

4.4.2 Micro-Vickers Hardness Test

Micro-Vickers hardness (MVH) test had been performed on top and cross-section side of the steel strip and recorded as shown in Table 4.8.

Table 4.8 Micro-Vickers Hardness (MVH) of Base ASSs

Section	**Micro-Vicker Hardness**			
	AISI 304	AISI 304L	201-2M	AISI 202
Top section	172.71 ± 2.01	186.60 ± 4.97	199.70 ± 5.80	191.01 ± 9.35
Cross-section	187.58 ± 8.36	192.97 ± 8.85	208.48 ± 2.71	195.18 ± 5.60

Tensile properties and MVH of 201-1M was presumed to be comparable to those of 201-2M. In general, grades 200 had higher tensile stress and MVH due possibly to the lower nickel content, whereas tensile strain of grades 300 was superior, as suggested in work of du Toit *et al*. (2012). Direction of cold-rolling was perpendicular to cross-section of the as-received sheet and could possibly introduced martensitic transformation as mentioned by Zhou *et al*. (2001) and de Abreu *et al*. (2007). MVH results in Table 4.8 indicated that cold-rolling affected steel hardness as higher MVH was found on cross-section. Higher MVH was found in 200s than as compared to 300s. Modified AISI 201 and 202 had lower SFE than those of AISI 304 and 304L, therefore they should have higher susceptibility to martensitic transformation when cold-rolling was applied. The results are in agreement with phase analysis by XRD showing martensite peaks.

4.5 Prediction of Structure Type and Solidification Mode and Weldments

Prediction of structure type in the weld zone and solidification mode of weldments has been made with reference to Kou (2003) and Lippold and Kotecki (2005) as given in Table 4.9. The predicted morphology of δ-ferrite dendrites in weldments of AISI 304, AISI 304L, 201-2M and AISI 202 is type B (mixed ferritic vermicular and lacy/lathy bundles with pack of austenitic grains) and FA solidification mode as shown by Suutala *et al*. (1980) and Elmer (1999). However, morphology prediction of 201-1M weldments is different. This steel has the lowest Cr_{eq}/Ni_{eq} ratio, hence structure type A and FA solidification mode are expected with slightly reduced amount of δ-ferrite.

Weld quality depends on the amount of δ-ferrite content. To maintain phases balance and proper ratio between austenite and ferrite phases, it should fall within a range of 3-10 to preserve the strength and corrosion resistance of welded steels as indicated in works of Lothongkum *et al*. (1999 and 2001), Lippold and Kotecki (2005) and Blondeu (2008). The δ-ferrite content of AISI 304 and AISI 304L falls within the optimum range, while that for the modified 201 ASSs exceeds the suggested range. Consequently, welding condition should introduce a small additional amount of nitrogen, as austenite promoter/stabilizer, during the welding process to lower the δ-ferrite content in the 200 ASSs as suggested by Iola et al. (1998).

Table 4.9 Calculated Parameters of Austenitic Stainless Steels

Calculations	**AISI 304**	**AISI 304L**	**201-1M**	**201-2M**	**AISI 202**
Cr_{eq}	19.3906	18.8463	19.3360	18.8833	15.7179
Ni_{eq}	11.3206	11.2318	16.0358	11.5453	10.4278
Cr_{eq}/Ni_{eq}	1.7129	1.6779	1.2058	1.6356	1.5073
$SFE\ (mJ/m^2)$	27.8842	27.4298	9.2870	8.1073	18.3944
$\delta - ferrite$	8.645	6.685	12.095	12.205	6.677
Structure Type and Solidification Mode Prediction of Weldments					
Possible type (*)	B	B	A	B	B
Possible mode (**)	FA	FA	FA	FA	FA

4.6 Dissolved Nitrogen in Weld Pool and Ferrite Content

Analysis results of dissolved nitrogen in weld pool and FN are compared with that in the base steel in Table 4.10 and Table 4.11, respectively. Nitrogen control in arc welding of stainless steels indicated that nitrogen content in weld metal of stainless steels, particularly those contained high nitrogen proportion (approximately 0.25 wt%) were not always governed by Sievert's law. To increase nitrogen proportion during welding of stainless steels are not always to increase nitrogen content in weld metal. Dissolution of nitrogen in weld metal is depends on the amounts of nitrogen and sulfur in base alloys composition as indicated in works of Kuwana *et al*. (1986), Du Toit and Pistorius (2003) and Spiedel (2006).

The nitrogen dissolution affected the change in FN at different nitrogen proportion ratio in shielding gas combined with their original nitrogen content during welding are showed in Figures 4.9 to 4.12. The increase in welding current influenced higher amount of nitrogen dissolution in AISI 304 weldment. FN was drastically decreased more than 50% when nitrogen was partially applied into shielding gas. Only under pure argon shielding gas that FN was still remained in the suggested range of 3 to 10. It was recommended by Deepashri *et al*. (2006) and Kim *et al*. (2011) to add nitrogen into shielding gas no more than 3 vol%. The influence of nitrogen proportion in shielding gas for AISI 304L weldment was as found in the case of AISI 304 weldment. For 201-2M weldment, the results are in agreement to those reported by Kuwana *et al*. (1986) and Morinari *et al*. (2008). An increase in welding current has a minor influence to the amount of nitrogen content of 201-2M weldment, but is significant to the decrease in the amount of FN as shown in Figure 4.11. The benefit from relatively higher nitrogen content in the as-received 201-2M and the nitrogen addition in shielding gas help to reduce the ferrite content in the weldment. Therefore, the optimum FN number in the range of 3 to 10 in 201-2M weldment was found under the N_2:Ar 5:95 shielding gas at the welding current of 130 A. For AISI 202 weldment, FN in weldment was much lower than that has been expected, either under pure argon or nitrogen-added shielding gas. The possible cause may be due to low content of chromium, which is a ferrite promoter, in the as-received base metal.

Table 4.10 Average Nitrogen Content in Different Weld Samples

Welding Current (A)/ ASS	**N in Base Metal**	**N in Weld Metal for Various Shielding Gas Composition**		
I = 130 A	GDS analysis	**N_2:Ar =0:100**	**N_2:Ar =5:95**	**N_2:Ar =10:90**
AISI 304	*0.0330*	0.0388	0.0422	0.1200
AISI 304L	*0.0590*	0.0583	0.0584	0.0127
201-2M	*0.2386*	0.1628	0.0522	0.0482
AISI 202	*0.0562*	0.0378	0.0556	0.0234
I = 160 A	GDS analysis	**N_2:Ar =0:100**	**N_2:Ar =5:95**	**N_2:Ar =10:90**
AISI 304	*0.0330*	0.0382	0.0489	0.0747
AISI 304L	*0.0590*	0.0582	0.0707	0.1114
201-2M	*0.2386*	0.1618	0.0665	0.0446
AISI 202	*0.0562*	0.0379	0.0268	0.0113

Table 4.11 Ferrite Contents as $\delta - ferrite$ and FN in ASS Weldment

FN at Weld Center Line (WCL)				
Details	**AISI 304**	**AISI 304L**	**201-2M**	**AISI 202**
Original $\delta - ferrite$	8.645	6.685	12.205	6.677
I = 130 Amp				
N_2:Ar =100:0	4.60	3.82	9.98	1.72
N_2:Ar =95:5	1.52	0.86	3.68	0.92
N_2:Ar =90:10	1.20	0.61	2.47	0.50
I = 160 Amp				
N_2:Ar =100:0	5.37	5.33	11.49	2.47
N_2:Ar =95:5	1.44	1.81	2.70	1.09
N_2:Ar =90:10	0.91	0.90	1.65	0.95

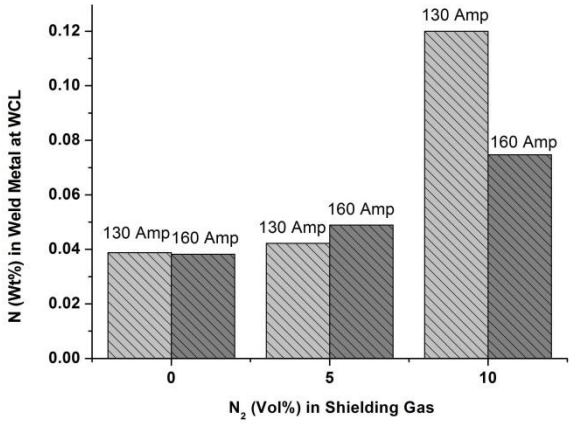

(a) Detected weight percentage of nitrogen at WCL

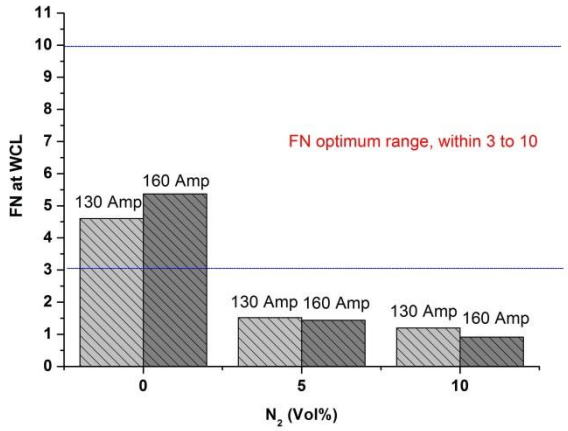

(b) FN in weld metal at WCL

Figure 4.9

(a) Detected weight percentage of nitrogen and (b) FN in weld metal of AISI 304 at different mixed ratio of N_2: Ar shielding gas at welding current 130 and 160 A

[wt% of N in the as-received AISI 304 = 0.0330 and predicted δ-ferrite = 8.645, recommended FN in weld metal should be in ranges of 3 to 10, WCL = weld center line]

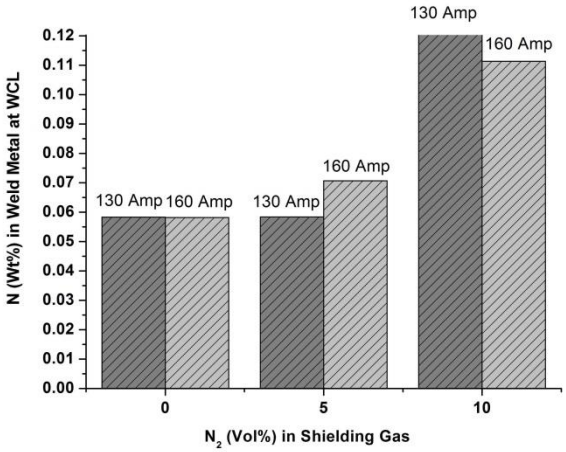

(a) Detected weight percentage of nitrogen at WCL

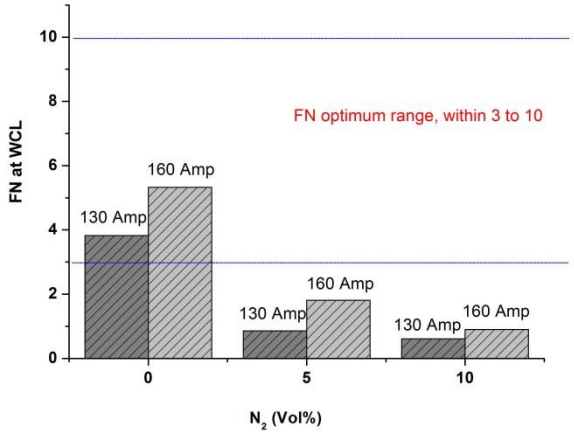

(b) FN in weld metal at WCL

Figure 4.10

(a) Detected weight percentage of nitrogen and (b) FN in weld metal of AISI 304L at different mixed ratio of N_2: Ar shielding gas at welding current 130 and 160 A

[wt% of N in the as-received AISI 304L = 0.0590 and predicted $\delta - ferrite$ = 6.685, recommended FN in weld metal should be in ranges of 3 to 10, WCL = weld center line]

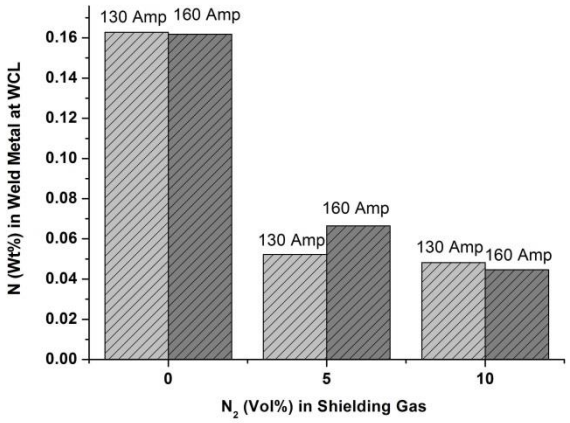

(a) Detected weight percentage of nitrogen at WCL

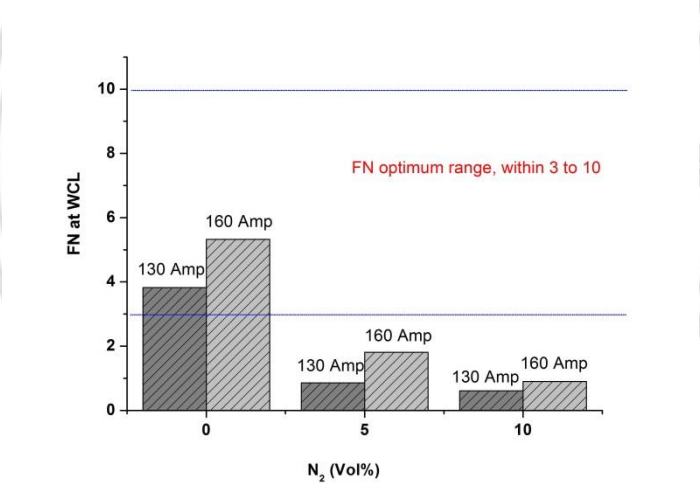

(b) FN in weld metal at WCL

Figure 4.11

(a) Detected weight percentage of nitrogen and (b) FN in weld metal of 201-2M at different mixed ratio of N_2: Ar shielding gas at welding current 130 and 160 A

[wt% of N in the as-received 201-2M = 0.2386, predicted $\delta - ferrite$ = 12.205, recommended FN in weld metal should be in ranges of 3 to 10, WCL = weld center line]

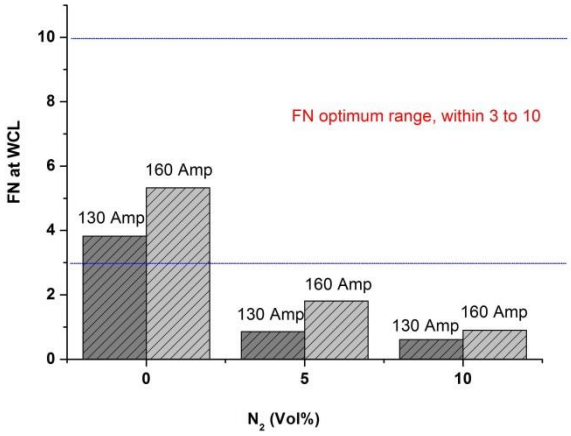

(b) FN in weld metal at WCL

Figure 4.12

(a) Detected weight percentage of nitrogen and (b) FN in weld metal of AISI 202 at different mixed ratio of N_2: Ar shielding gas at welding current 130 and 160 A

[wt% of N in the as-received AISI 202 = 0.0562, predicted $\delta - ferrite$ = 6.677, recommended FN in weld metal should be in ranges of 3 to 10, WCL = weld center line]

4.7 Weld Pool Inspection

Inspection data on weld geometry are shown in Figures 4.13 to 4.16. From optical microscopy, neither gas bubble nor trace of cracks was found. Calculation of penetration depth ratio is given in Appendix B. With the controlled welding parameters set up in this work, the applied welding current at 130 A could not achieve completed penetration for PCGTAW AISI 304. The best obtained weld-bead geometry was found at the applied welding current at 160 A under pure argon shielding gas. Welding current at 160 A led to a larger weld front and over penetration depth as seen in Figure 4.13(a). The increase in welding current rendered the over-complete penetration and increase the curvature at top and bottom of weld work. Generally, proportion of front width length to penetration depth should be appear in symmetry to each other as illustrated in Figure 4.13. The increasing amount of nitrogen has no significance to the front width of weld beads as appeared in the plot of Figure 4.13(c). Weld pool geometry inspection of PCGTAW AISI 304L (Figure 4.14) fabricated under 5 and 10 Vol% nitrogen-argon balance shielding gas appeared in quite distort appearance and may affect mechanical properties. Weld plates at welding current 160 A showed more distorted geometry than at 130 A. Combination of drastic reduction in FN due to nitrogen dissolution into weld metal and distorted weld pool geometry should detrimentally affect mechanical properties of PCGTAW AISI 304 and 304L. The weld geometry inspection of PCGTAW 201-2M (Figure 4.15) was similar to those with low nickel, high nitrogen and low sulfur austenitic stainless steels. Weld pool geometry became unbalance in the proportion of front width to penetration depth at the welding current 160 A. Best symmetric width-to-depth was exhibited at the welding current 130 A under $5N_2$:95Ar shielding gas. For PCGTAW AISI 202, symmetric width-to-depth geometry was also exhibited at welding current 130 A under 5N2:95Ar shielding gas (Figure 4.16).

Consequently, the inspection results indicated that to fabricate 2 mm thick ASSs by PCGTAW process, the appropriate applied welding current should be 130 A for 201-2M and AISI 202 and 160 A for AISI 304 and AIS 304L.

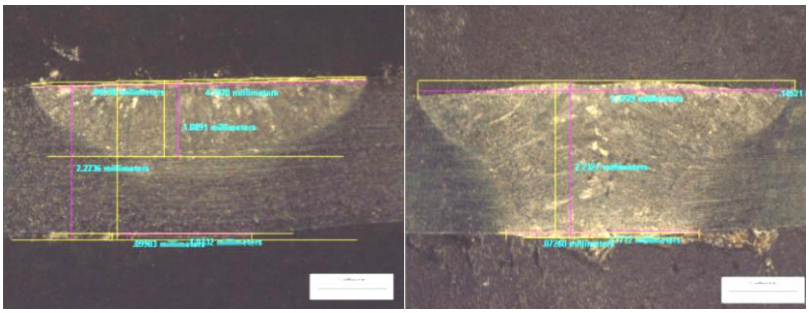

(a)130 A (b) 160 A

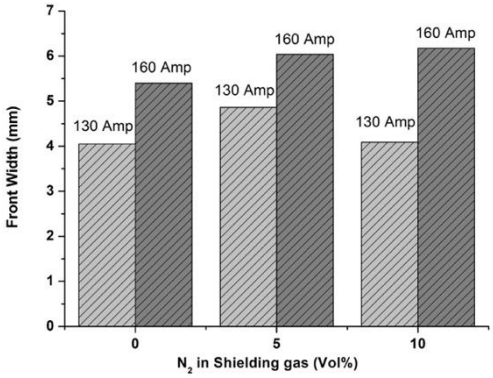

(c) Front width at N_2 in shielding gas = 0, 5 and 10

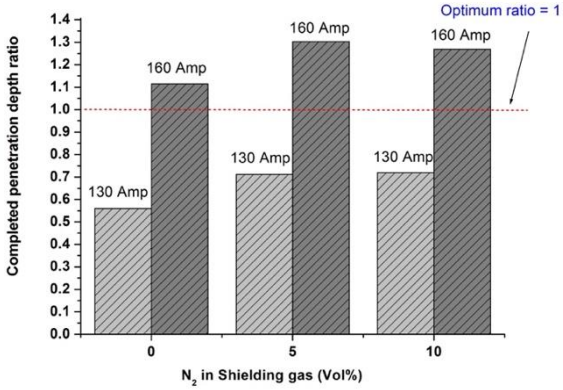

(d) Completed penetration depth ratio at N_2 in shielding gas = 0, 5 and 10

Figure 4.13 (a), (b) Weld pool inspection of PCGTAW AISI 304, shielding gas ratio N_2:Ar = 0:100, (c) weld pool front width and (d) completed penetration depth at welding current 130 and 160 A, respectively

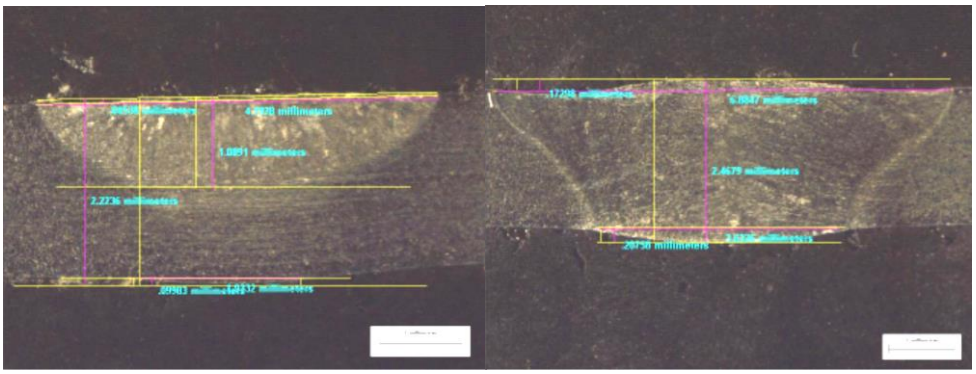

(a)130 A (b) 160 A

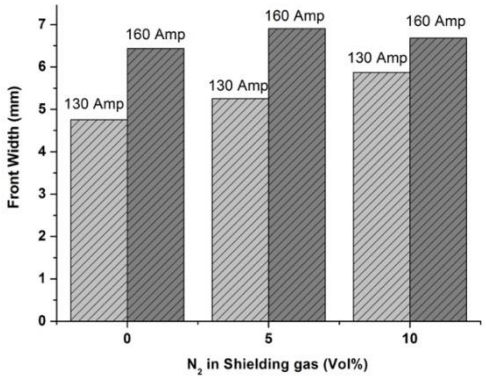

(c) Front width at N_2 in shielding gas = 0, 5 and 10

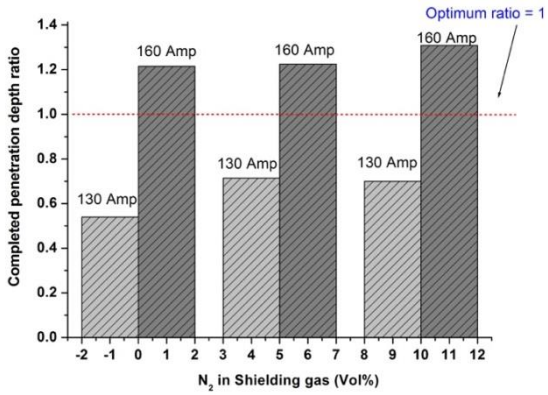

(d) Completed penetration depth ratio at N_2 in shielding gas = 0, 5 and 10

Figure 4.14 (a), (b) Weld pool inspection of PCGTAW AISI 304L, shielding gas ratio N_2:Ar= 0:100 and 5:95 (c) weld pool front width and (d) completed penetration depth at welding current 130 and 160 A, respectively

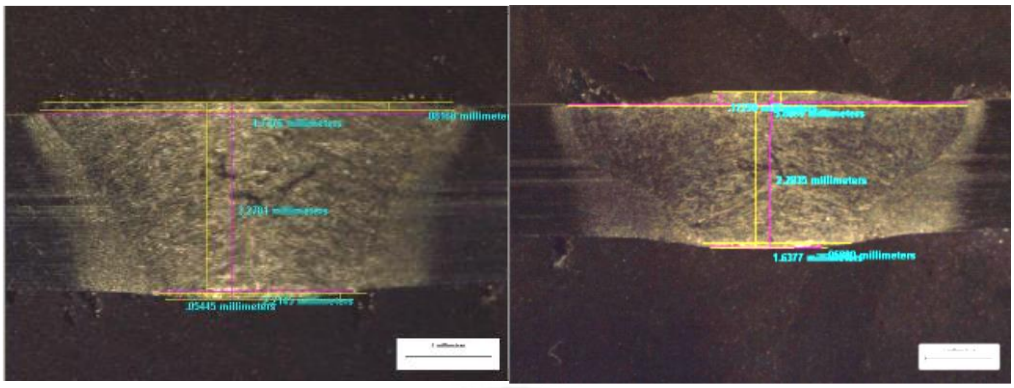

(a)130 A (b) 160 A

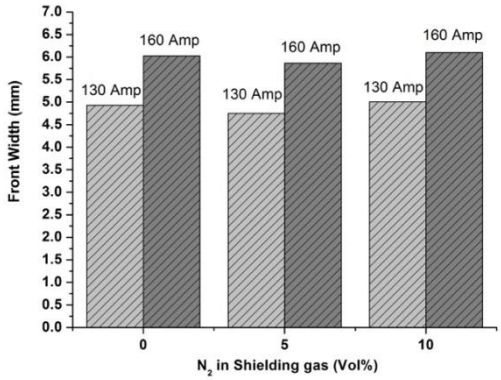

(c) Front width at N_2 in shielding gas = 0, 5 and 10

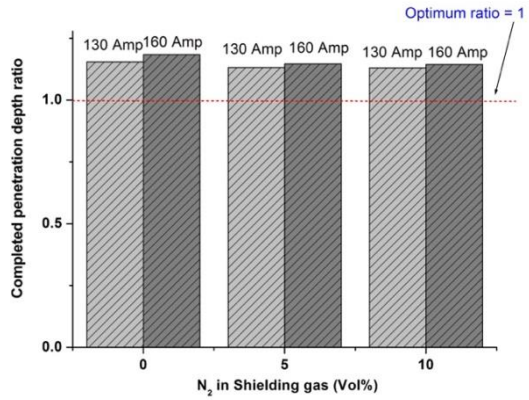

(d) Completed penetration depth ratio at N_2 in shielding gas = 0, 5 and 10

Figure 4.15 (a), (b) Weld pool inspection of PCGTAW 201-2M, shielding gas ratio N_2:Ar = 5:95, (c) weld pool front width and (d) completed penetration depth at welding current 130 and 160 A, respectively

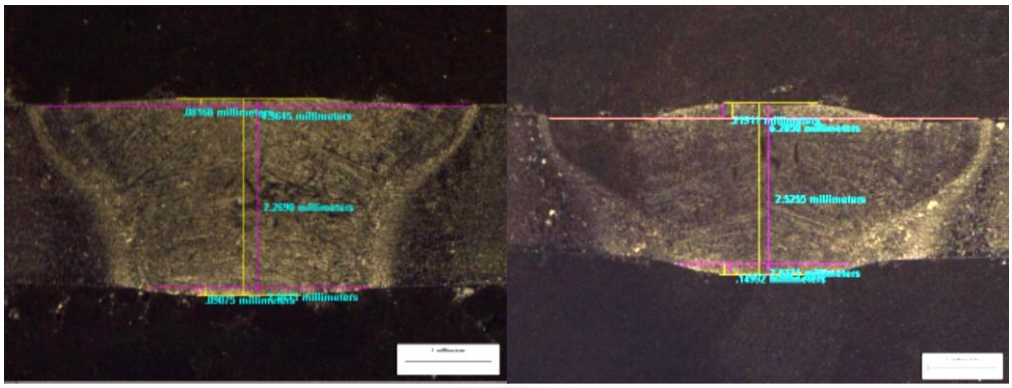

(a)130 A (b) 160 A

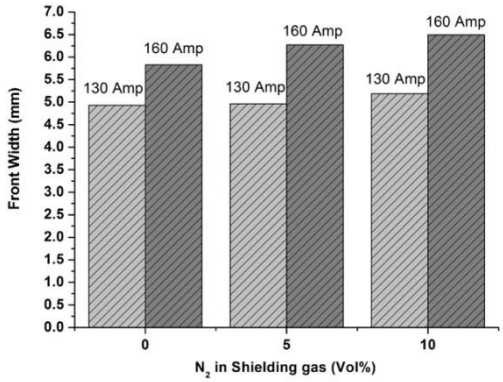

(c) Front width at N_2 in shielding gas = 0, 5 and 10

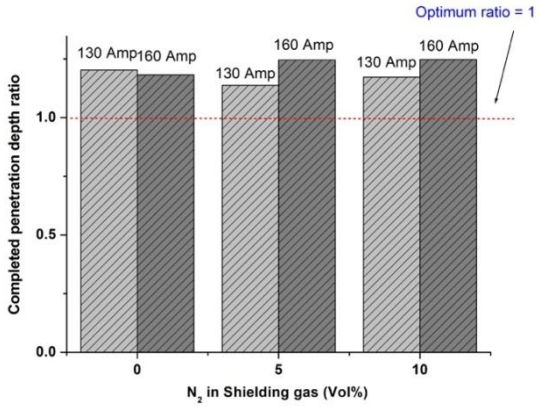

(d) Completed penetration depth ratio at N_2 in shielding gas = 0, 5 and 10

Figure 4.16 (a), (b) Weld pool inspection of PCGTAW AISI 202, shielding gas ratio N_2:Ar = 5:95, (c) weld pool front width and (d) completed penetration depth at welding current 130 and 160 A, respectively

4.8 Pitting Corrosion Resistance (PCR) of Weldment

Calculation of E_P, (E_b - E_P), E_{corr} and I_{corr} at different applied welding currents and shielding gas was summarized in Tables 4.12 and 4.13. Influence of change in E_P to pit width and site distribution was plotted in Figure 4.17. Plots of CVs and pit morphology of each weldment were shown in Figures 4.18 to 4.25.

Table 4.12 Calculation on Pitting Corrosion Resistance at I=130 A

Base	E_p $mV\ vs\ SCE$	$E_b - E_p$ $mV\ vs\ SCE$	E_{corr} $mV\ vs\ SCE$	I_{corr} $(\mu A/cm^2)$
AISI 304	*212*	*208*	*-947*	*-4.950*
0N_2:100Ar	135	593	-864	7.940
5N_2:95Ar	575	788	-963	3.900
10N_2:90Ar	574	785	-914	1.896
AISI 304L	*211*	*132*	*-970*	*6.872*
0N_2:100Ar	528	746	-990	4.522
5N_2:95Ar	515	732	-936	6.295
10N_2:90Ar	514	738	-938	5.306
201-2M	*144*	*253*	*-944*	*7.738*
0N_2:100Ar	475	720	-659	5.812
5N_2:95Ar	528	752	-609	2.355
10N_2:90Ar	341	645	-683	6.921
AISI 202	*149*	*47*	*-1004*	*5.922*
0N_2:100Ar	332	332	-774	3.890
5N_2:95Ar	675	675	-735	3.351
10N_2:90Ar	293	293	-769	4.168

Table 4.13Calculation on Pitting Corrosion Resistance at I=160 A

Base	E_p $mV\ vs\ SCE$	$E_b - E_p$ $mV\ vs\ SCE$	E_{corr} $mV\ vs\ SCE$	I_{corr} $(\mu A/cm^2)$
AISI 304	*212*	*208*	*-947*	*-4.950*
0N_2:100Ar	653	863	-596	4.714
5N_2:95Ar	572	783	-914	2.061
10N_2:90Ar	572	805	-828	7.279
AISI 304L	*211*	*132*	*-970*	*6.872*
0N_2:100Ar	512	733	-939	2.305
5N_2:95Ar	506	727	-958	2.555
10N_2:90Ar	513	773	-843	2.225
201-2M	*144*	*253*	*-944*	*7.738*
0N_2:100Ar	1431	1124	-578	1.847
5N_2:95Ar	828	1051	-731	1.505
10N_2:90Ar	1204	1370	-691	1.042
AISI 202	*149*	*47*	*-1004*	*5.922*
0N_2:100Ar	887	1158	-796	0.356
5N_2:95Ar	635	1133	-855	7.725
10N_2:90Ar	1313	1625	-789	2.558

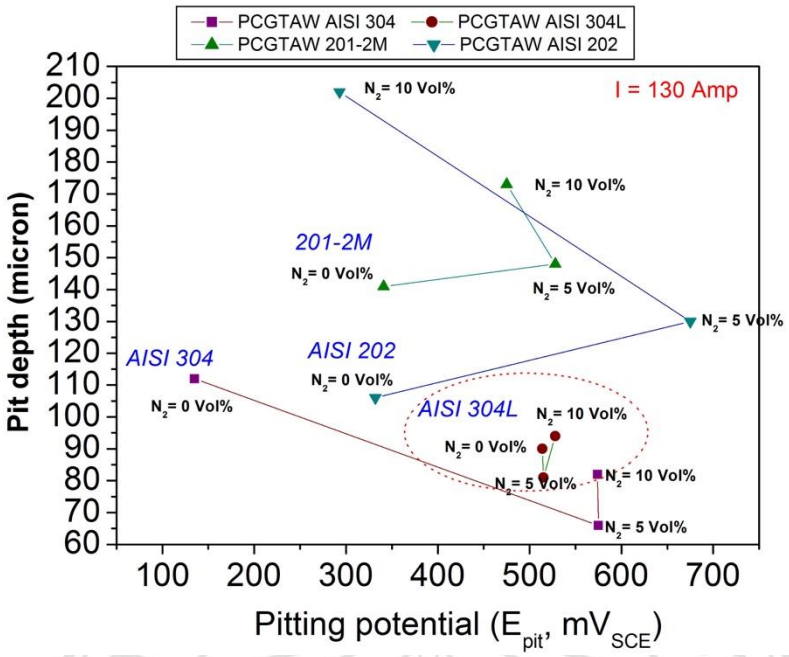
PCGTAW AISI 304
PCGTAW AISI 304L
PCGTAW 201-2M
PCGTAW AISI 202
I = 130 Amp
Pit depth (micron)
Pitting potential (E_pit, mV_SCE)
201-2M
AISI 304
AISI 202
AISI 304L
N2= 10 Vol%
N2= 5 Vol%
N2= 0 Vol%

(a)

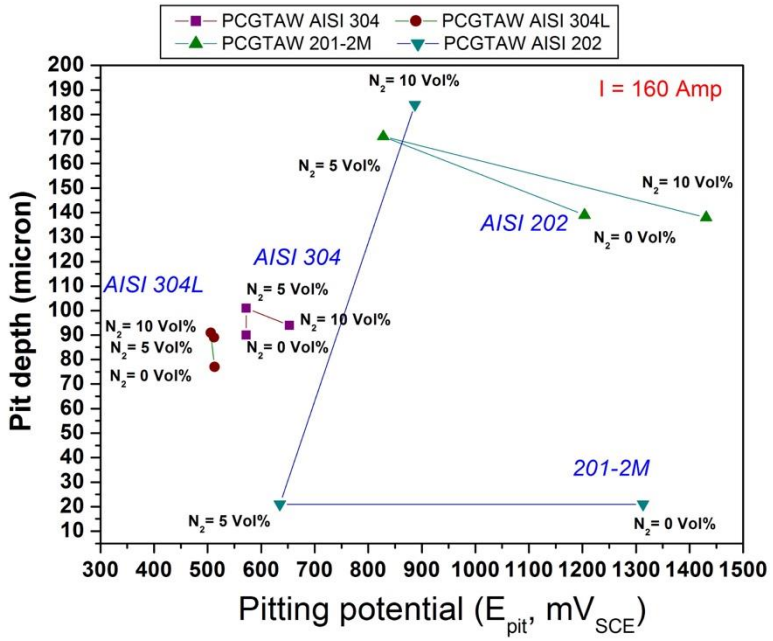
PCGTAW AISI 304
PCGTAW AISI 304L
PCGTAW 201-2M
PCGTAW AISI 202
I = 160 Amp
Pit depth (micron)
Pitting potential (E_pit, mV_SCE)
AISI 202
AISI 304
AISI 304L
201-2M
N2= 10 Vol%
N2= 5 Vol%
N2= 0 Vol%

(b)

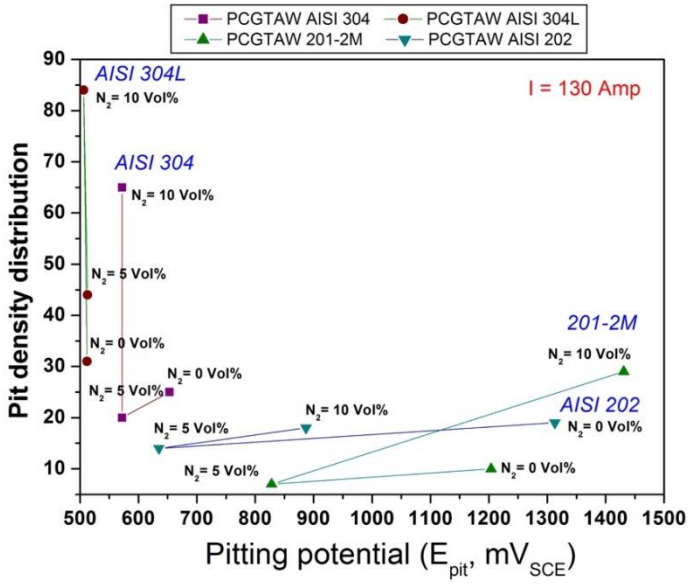

(c)

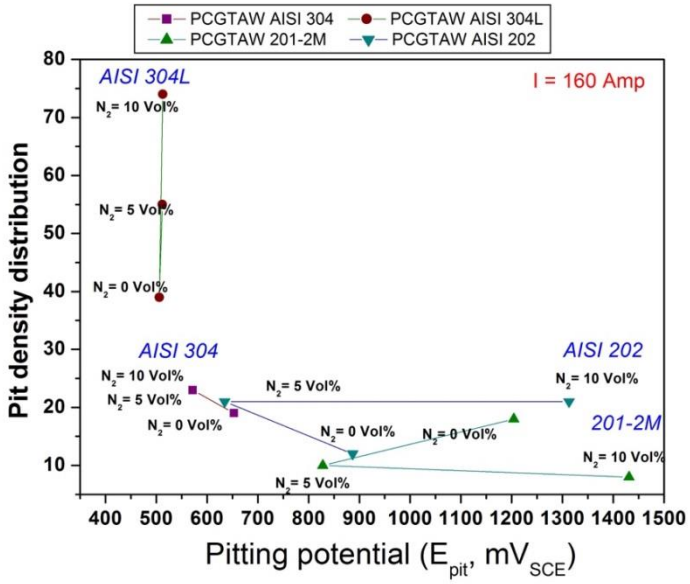

(d)

Figure 4.17 (a) and (b) pit depth in the observed area across weld specimen with change in pitting potentials at different welding currents and under various mixed shielding gases, (c) and (d) pit density distribution in the observed area across weld specimen with change in pitting potentials at different welding currents and under various mixed shielding gases.

4.8.1 PCGTAW AISI 304

At welding current 130 A, pitting corrosion potential (E_P) was obtained from polarization curves under an influence of different amount of nitrogen in shielding gases in Figure 4.19. The obtained corrosion potential from Tafel plots (E_{corr}) were shifted slightly toward the negative region with a reduction in corrosion current density (I_{corr}) when the amount of nitrogen proportion in shielding gases was increased. Pitting potential of welded AISI 304 under pure argon gas was lower than that of the base AISI 304 (E_P = 210 mV_{SCE}). The higher amount of nitrogen proportion in shielding gases has an influence on the susceptibility to pitting corrosion. The results are in agreement with those observed by Jargelius-Petterson (1999). The average pit depth found was deeper than those under the 5 and 10 Vol% N_2: Ar shielding gas (Figure 4.18). The distribution of pit sites was found to increase as plotted in Figure 4.17, depending on pitting potential (E_P).

Comparison to the case at 160 A, nitrogen still has a negative effect on pitting corrosion resistance. E_P, $E_{corr}$and (E_b - E_P) were decreased with increasing amount of nitrogen in shielding gases.

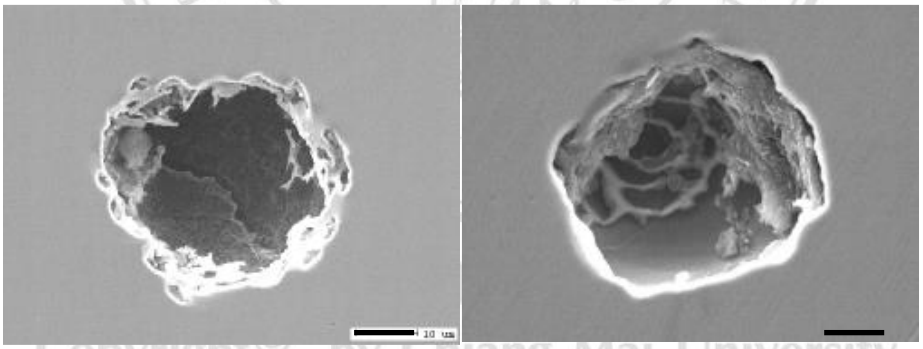

Welding current 130 A, 0N_2:100Ar Welding current 160 A, 0N_2:100Ar

Figure 4.18 Pit morphology of PCGTAW AISI 304

Note: micron marker = 20 microns

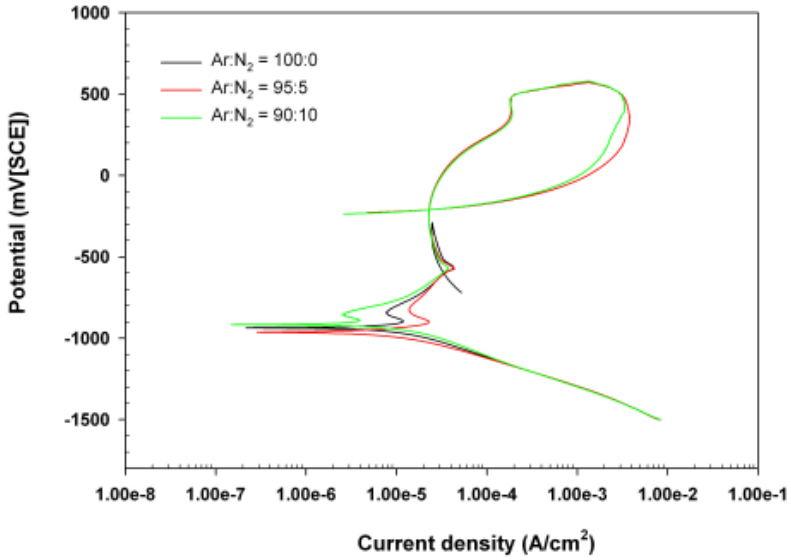

Welding current 130 A

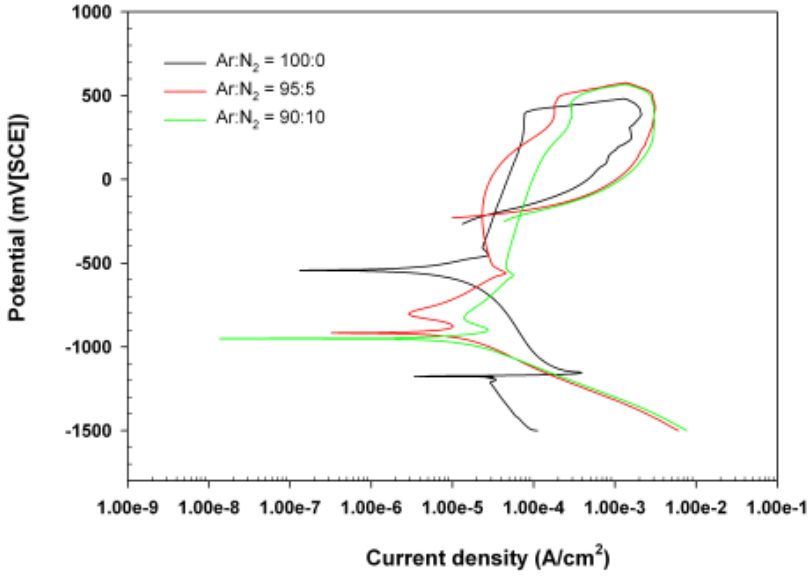

Welding current 160 A

Figure 4.19 CV potentiodynamic polarization curves of PCGTAW AISI 304 at welding current 130 and 160 A under various ratio of N_2:Ar shielding gases.

4.8.2 PCGTAW AISI 304L

From polarization curves in Figure. 4.21, E_{corr} was shifted toward noble region with an increase of nitrogen content at both welding currents, 130 and 160 A. This was similar what has been described for the case of PCGTAW AISI 304. The difference in the obtained E_{corr} and (E_b - E_P) between welded AISI 304 and AISI 304L under pure argon shielding gas should be a result from the amount of chromium content. AISI 304 contains higher amount of chromium than AISI 304L and the amount of carbon in AISI 304L was also higher than that recommended in the standardization, hence better pitting corrosion resistance was observed in AISI 304L weldment. It was recommended by Lippold and Savage (1982) and Gooch (1996) that nitrogen addition in conventional GTAW process of series 300s should not be generally higher than 2%. The results from the present work on pitting corrosion resistance of PCGTAW AISI 304 and AISI 304L under mixed nitrogen-argon shielding gases were in agreement.

Overall, pitting corrosion resistance of both PCGTAW 300s are better than that of the 200s. Optimum welding current for the 300s should be at 160 A.

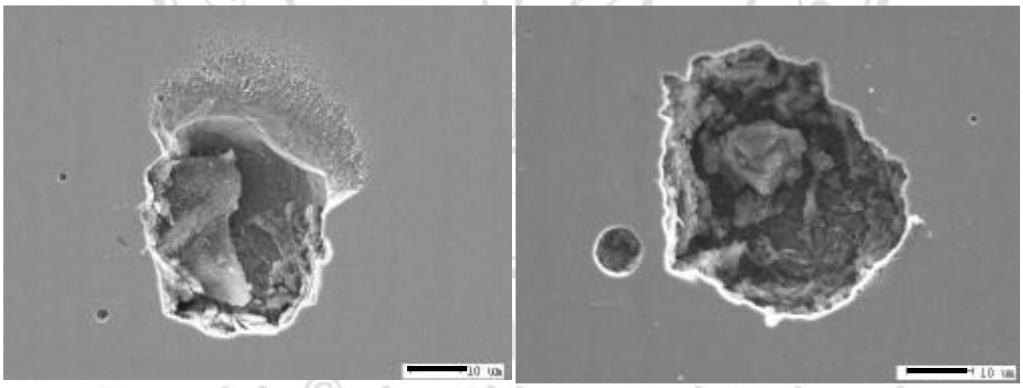

Welding current 130 A, $0N_2$:100Ar Welding current 160 A, $0N_2$:100Ar

Figure 4.20 Pit morphology of PCGTAW AISI 304L

Note: micron marker = 10 microns

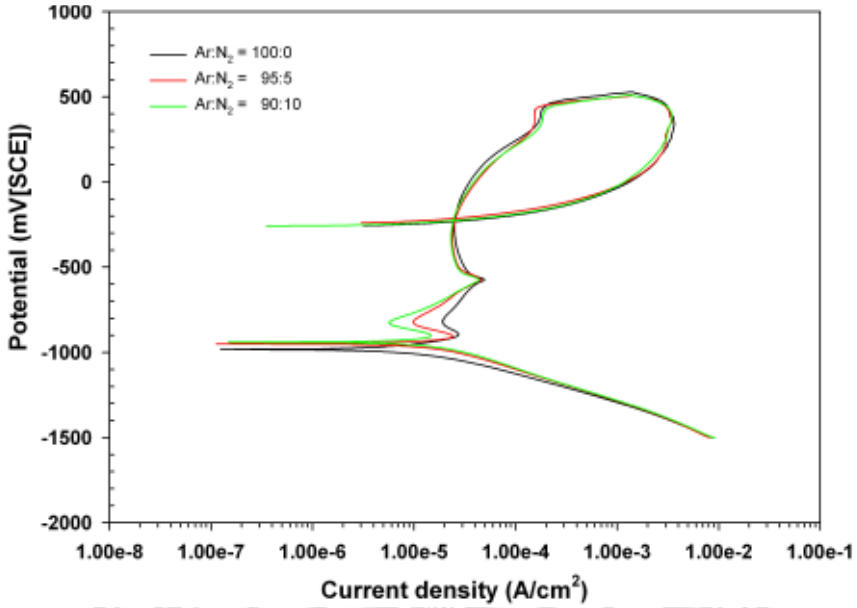

Welding current 130 A

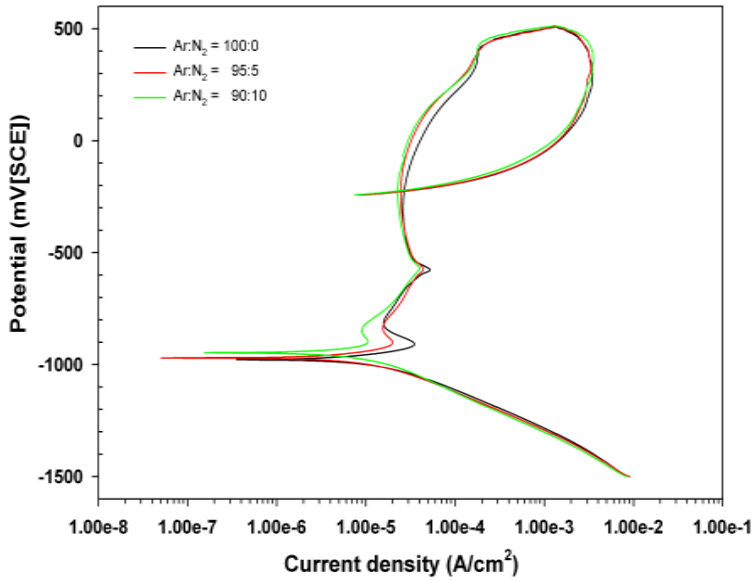

Welding current 160 A

Figure 4.21 CV potentiodynamic polarization curves of PCGTAW AISI 304L at welding current 130 and 160 A under various ratio of Ar:N_2 shielding gases.

4.8.3 PCGTAW 201-2M

Elemental composition analysis and weld pool geometry inspection have revealed that 201-2M can be classified in a different category from AISI 304, AISI 304L and AISI 202. Nitrogen addition increased noble corrosion potential for nearly 40 % than was found in its parent steel with the 5 N_2:95Ar shielding gases at the applied welding current 130 A as seen in Figure. 4.23. At welding current 160 A, E_P and (E_b - E_P) were moved toward more negative potential region. Although the average pit depth in Figure 4.17 at 5 Vol% nitrogen shielding gases was shallower than the rest, but the pit site distribution was not improved. Comparison between pit morphology at the different welding currents was in Figure 4.22. In general, the addition of 5 Vol% nitrogen into shielding gases can help to improve pitting corrosion resistance of PCGTAW 201-2M when applied welding current was at 130 A, as has been suggested by Gooch (1996). However, nitrogen absorption and desorption behavior in PCGTAW 201-2M did not follow Sievert's law. Therefore, addition of nitrogen into shielding gases for more than 5 Vol% with the present controlled welding parameters for 201-2M is not necessary. This is in agreement to previous works by Kuwana*et al*. (1986), Iorio*et al*. (1994) and Du Toit and Pistorius (2003).

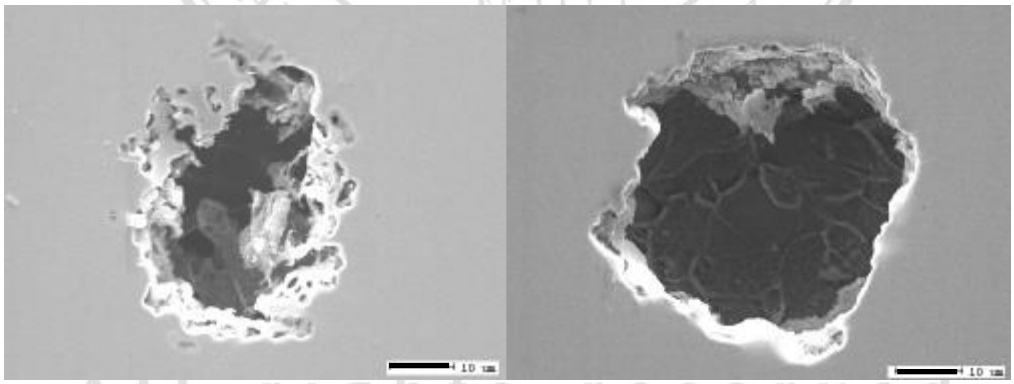

Welding current 130 A, 0N_2:100Ar Welding current 160 A, 0N_2:100Ar

Figure 4.22 Pit morphology of PCGTAW 201-2M

Note: micron marker = 10 microns

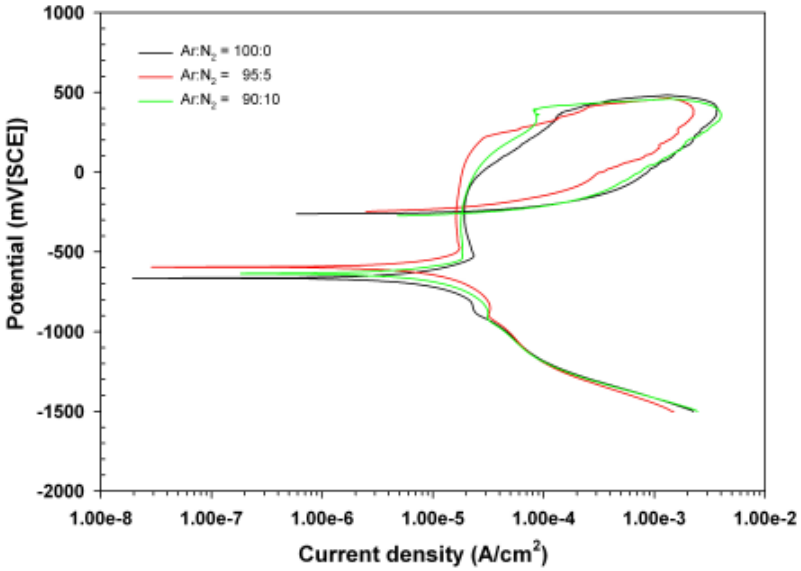

Welding current 130 A

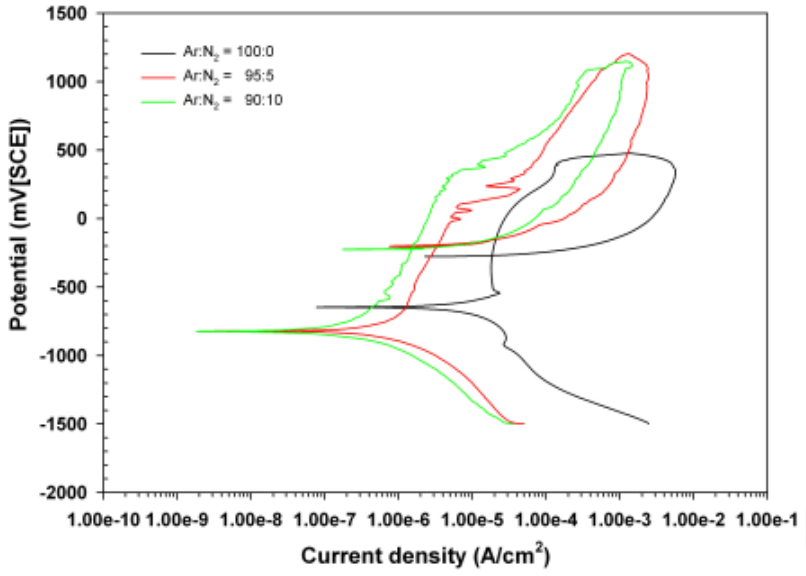

Welding current 160 A

Figure 4.23 CV potentiodynamic polarization curves of PCGTAW 201-2M at welding current 130 and 160 A under various ratio of $Ar:N_2$ shielding gases.

4.8.4 PCGTAW AISI 202

E_{corr} of PCGTAW AISI 202 in Figure 4.25 tended toward noble potential with increasing amount of nitrogen proportion in shielding gases, but it was not as remarkable as found in the case of 201-2M. This can be a result from relatively lower chromium content in the as-received base metal than recommended standardization. Welding current at 130 A was the optimum setting for the PCGTAW AISI 202. Under $5N_2$:95Ar shielding gases, shallow pit depth and less pit site distribution across weld surface implied an improvement in pitting corrosion resistance as pit morphology in Figure 4.24.

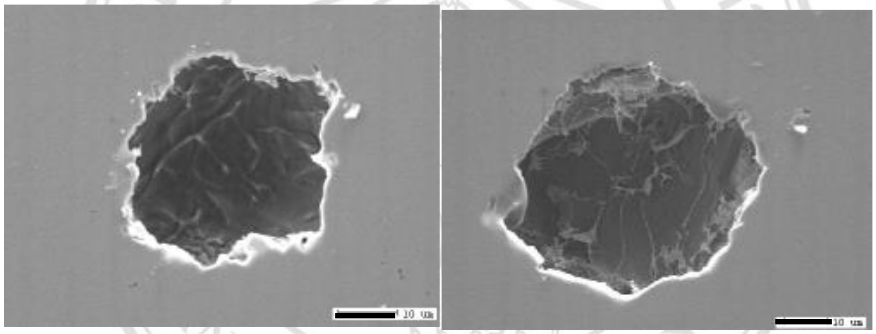

Welding current 130 A, $0N_2$:100Ar Welding current 160 A, $0N_2$:100Ar

Figure 4.24 Pit morphology of PCGTAW AISI 202

Note: micron marker = 10 microns

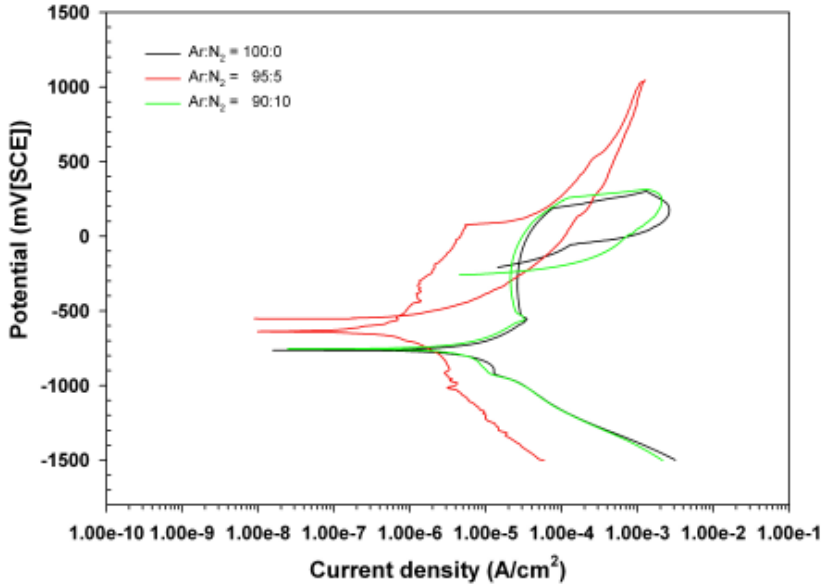

Welding current 130 A

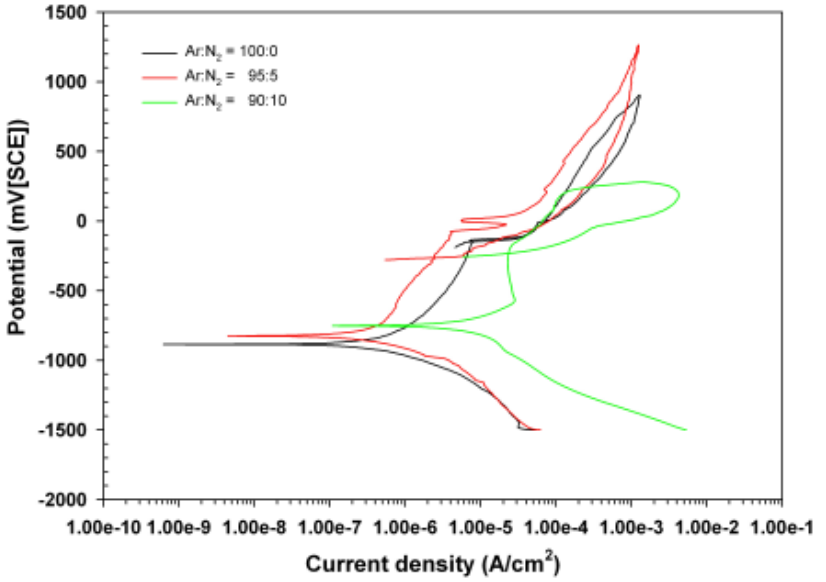

Welding current 160 A

Figure 4.25 CV potentiodynamic polarization curves of PCGTAW AISI 202 at welding current 130 and 160 A under various ratio of Ar:N_2 shielding gases

From the plots between pitting potential and pit morphology in Figure 4.17, there are two factors for improving pitting corrosion resistance of weld specimens:

1. Welding current
2. Nitrogen proportion in shielding gases

To achieve an improvement in pitting corrosion resistance, the concentration of nitrogen, partially mixed with argon gas, should not exceed 2 Vol.% for AISI 304 and AISI 304L and 5 vol.% for 201-2M and AISI 202. The optimum welding current should be 130 A for 201-2M and AISI 202, and 160 A for AISI 304 and AISI 304L. Nitrogen addition to shielding gases can improve pitting corrosion resistance of 201-2M to a similar level as that of AISI 304. Consequently, 201-2M can be a potential candidate for pipeline applications in mild chloride-containing environment.

4.9 Degree of Sensitization of Weldment

DOS results of the as-received base metal indicated that 201-2M and AISI 202 have higher susceptibility to corrosion attack at grain boundaries than that of AISI 304 and AISI 304L. To improve corrosion resistance of the 200s series to the same level of the 300s series, nitrogen had partially introduced into the shielding gas during the welding. There is a possibility that nitrogen can form a film of (C+N) that helped to increase thickness of passive film and resulted in an improvement of corrosion resistance (Moon *et al*., 2013), particularly for PCGTAW 201-2M and AISI 202.

4.9.1 PCGTAW AISI 304

DLEPR plots in Figure 4.26 showed significant decrease in activation and reactivation current when nitrogen had been added in shielding gases. In potential range 0 to –300 mV SCE, dominant donor species in this region could possibly be oxygen vacancies as stated by Ha *et al*. (2009) during the passive film dissolution. Only mild attack was found at grain boundary of base zone (BZ) in PCGTAW AISI 304.

Susceptibility to sensitization was increased with increasing welding current. Comparison among the original DOS of base metal to that obtained from weld metal in Table 4.14 indicated that sensitization at grain boundaries increased when the amount of nitrogen in shielding gases was increased under the applied welding current of 130 A. Higher welding current at 160 A, sensitization was not significantly affected by an increase in the amount of nitrogen. There was a possibility that some minor alloying elements in base AISI 304 such as Mo or even Cr might react with the excess nitrogen in shielding gases resulting in detrimental nitride compounds and chromium depletion that increase susceptibility to intergranular corrosion.

Nitrogen in the shielding gas affected weld solidification as several elongate dendrites were found in FZ at the edge of typical FA mode, which was the mixed dendritic structures of lacey and vermicular ferrites. Weld solidification mode in FZ of PCGTAW AISI 304 was mainly FA mode and there was a minority of A (austenite) mode which contained higher nitrogen proportion than that in typical FA mode at the adjacent boundary of FZ to HAZ. Mild sensitized zone was found at the boundary between BZ to

HAZ and at twin grain boundaries. At the distance further than 2 mm toward WCL, there were almost no sensitized grains. The change in DOS in weld metal was higher than that was found in base AISI 304 around 50%.

Comparison of the applied shielding gas between pure argon and partially mixed with nitrogen to PCGTAW AISI 304 with welding current at 130 and 160 A found that nitrogen led to lower susceptibility to corrosion attack at grain boundary. If nitrogen had uniformly distributed over the surface, Cr or Mo nitrides film can form and contributed to passivation kinetics and increased strength of passive layer resulting in reduced susceptibility to sensitization (Olefjord and Wegrelius, 1996 and Metikoš-Huković *et al*., 2011).

Under Ar:N_2 = 95:5 shielding gas

Welding Current 130 A

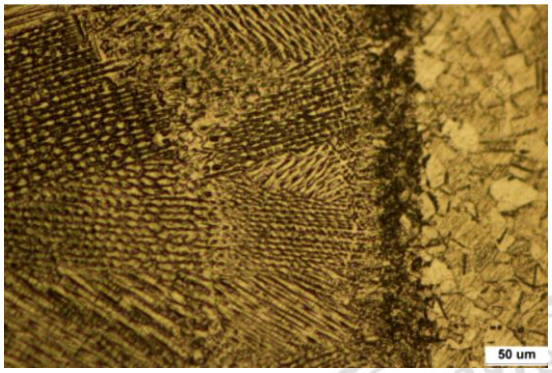

Welding Current 160 A

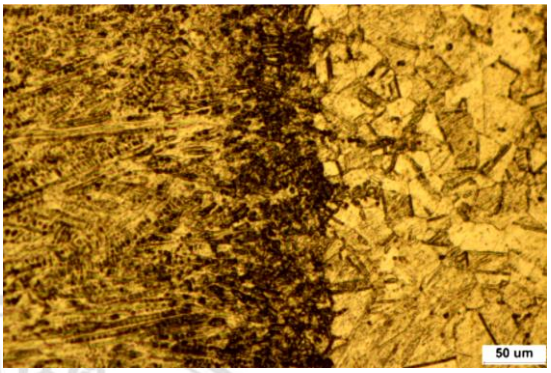

FZ → HAZ

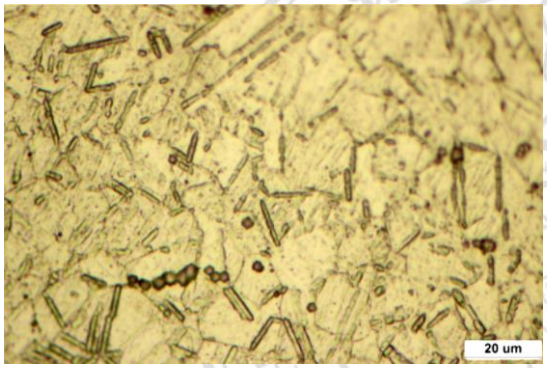

FZ → HAZ

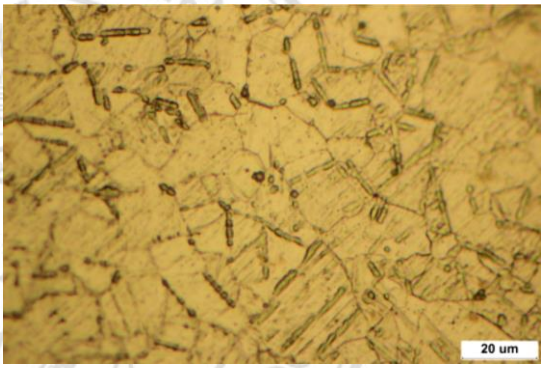

BZ mildly sensitized

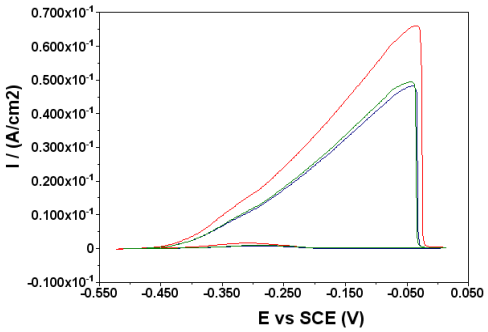

BZ mildly sensitized

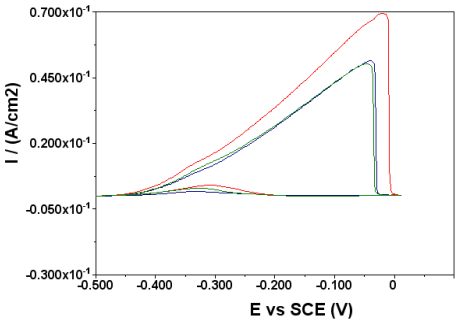

DLEPR Plots

DLEPR Plots

Mixed ratio of shield gases indicated by color as:

Red- Ar:N_2 =100: 0, Blue- Ar:N_2 = 95:5, Green- Ar: N_2 = 90:10

Figure 4.26 Grain boundary morphology of sensitized PCGTAW AISI 304 and DLEPR plots at welding current 130 and 160 A under 5N_2:95Ar

Table 4.14 DOS of PCGTAW AISI 304

Welding current (Amp)/ N_2:Ar	$I_a(\mu A/cm^2)$	$I_r(\mu A/cm^2)$	**DOS**(I_r/I_a)	**% change in DOS**
130 A				
$0N_2$:100Ar	5.255E-02	1.073E-03	2.028E-02	18.70
$5N_2$:95Ar	4.802E-02	3.803E-04	7.870E-03	8.46
$10N_2$:90Ar	2.480E-02	4.403E-04	8.481E-01	44.00
160 A				
$0N_2$:100Ar	6.668E-02	3.474E-03	5.209E-02	50.63
$5N_2$:95Ar	6.275E-02	1.781E-03	2.868E-02	41.74
$10N_2$:90Ar	6.407E-02	2.009E-03	3.130E-02	44.72

4.9.2 PCGTAW AISI 304L

Micrographs observation (Figure 4.27) indicated the presence of FA mode as found in weld metal of PCGTAW AIS 304. No abnormally grain growth at the partially melted zone and no appearance of hot crack trace along weld seam and at HAZ. The addition of nitrogen in shielding gases seemed to have positive effect and enhance its corrosion resistance as compared with pure argon gas. No severe attack at grain boundary was found.

Since compositions of AISI 304 and AISI 304L are quite similar as well as the calculated SFE values, therefore their IGC behavior was almost in similarity. The integrated areas of DOS curves with nitrogen in mixed shielding gas were a bit higher than those with pure argon gas. At welding current 160 A, the obtained DOS results indicated that an increase in welding current not only help to improve weld pool geometry and given completed penetration seam, but also improve resistance to sensitization.

Under Ar:N2 = 95:5 shielding gas

Welding Current 130 A

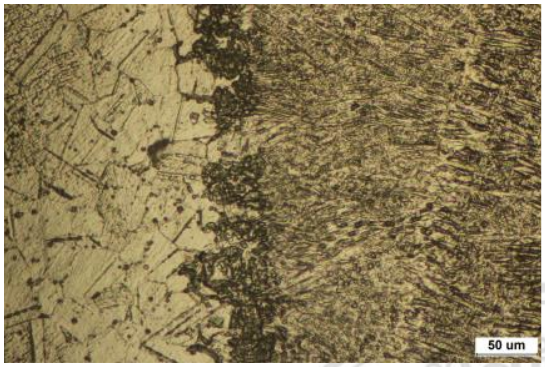

FZ → HAZ

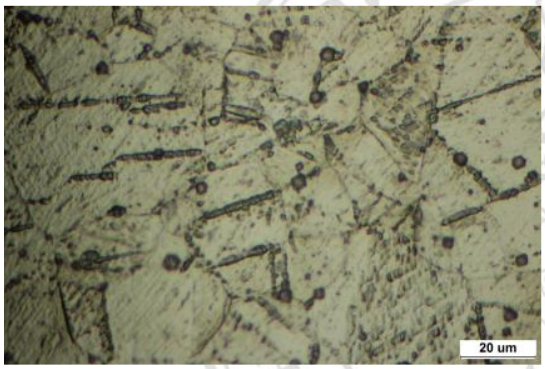

BZ mildly sensitized

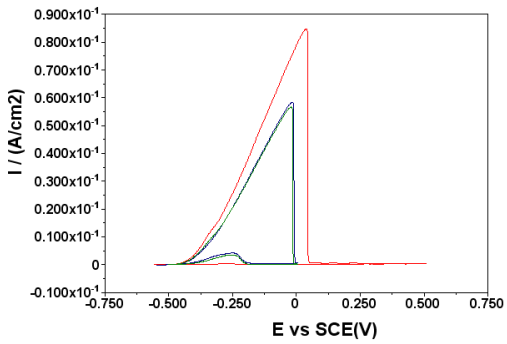

DLEPR Plots

Welding Current 160 A

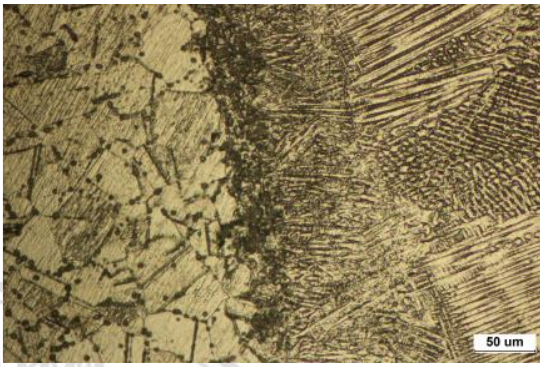

FZ → HAZ

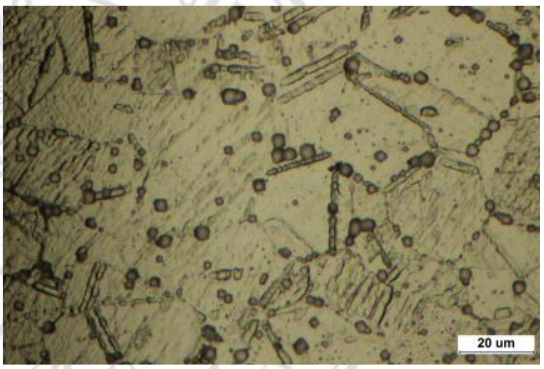

BZ mildly sensitized

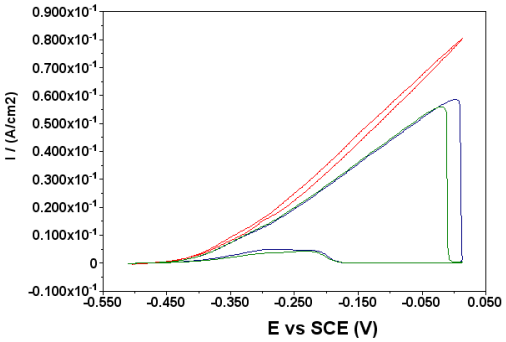

DLEPR Plots

Mixed ratio of shield gases indicated by color as:

Red- Ar:N_2 =100: 0, Blue- Ar:N_2 = 95:5, Green- Ar: N_2 = 90:10

Figure 4.27 Grain boundary morphology of sensitized PCGTAW AISI 304L and DLEPR plots at welding current 130 and 160 A under 5N_2:95 Ar

Table 4.15 DOS of PCGTAW AISI 304L

Welding current (Amp)/ N_2:Ar	$I_a(\mu A/cm^2)$	$I_r(\mu A/cm^2)$	**DOS**(I_r/I_a)	**% change in DOS**
130 A				
$0N_2$:100Ar	6.653E-02	0.000E+00	0.000E+00	47.38
$5N_2$:95Ar	5.604E-02	4.007E-03	7.152E-02	24.15
$10N_2$:90Ar	5.506E-02	3.536E-03	6.431E-02	21.98
160 A				
$0N_2$:100Ar	6.668E-02	3.474E-03	5.209E-02	14.15
$5N_2$:95Ar	6.275E-02	1.781E-03	2.868E-02	7.41
$10N_2$:90Ar	6.407E-02	2.009E-03	3.130E-02	9.67

4.9.3 PCGTAW 201-2M

The obtained DLEPR results of PCGTAW 201-2M were different from those of AISI 304 and AISI 304L as shown in Figure 4.28. The reaction was appeared to have more activity than the repassivation kinetics from iron dissolution during the applied reverse scan potential. Therefore, the possible assumption for the activities in zone I and II should be as follows. The first zone (zone I) appeared in the applied potential range of –100 to -350 mV_{SCE}. It was created by oxygen vacancies during the passivation from iron spinel dissolution as normally found in the results of PCGTAW AISI 304 and 304L as well as in the work by Ha *et al*. (2009). The second zone (zone II) was started at potential -350 to -450 mV_{SCE} and was suspected that it was a contribution from the ion density of the second donor [C+N] species formation. High carbon and nitrogen content can possibly provide support and strengthening to the chromium protective film.

Table 4.16 showed a decrease in susceptibility to sensitization. In general, the base metal 201-2M has higher amounts of nitrogen and carbon in the composition more those of others. Therefore, after the weld solidification was completed, nitrogen could affect the charge ionization mechanism of Cr (VI) ions. It was postulated that, at potential range of 0.224 to 0.294 VSCE, compounds of carbon and nitrogen has been formed as film. This [C+N] passive film can help to increase film thickness and chromium concentration, hence protecting metal dissolution. Therefore, reduction in DOS was found in PCGTAW 201-2M and nitrogen in shielding gas can help to improve corrosion resistance at grain boundary during welding of PCGTAW 201-2M.

Under Ar:N2 = 95:5 shielding gas

Welding Current 130 A | Welding Current 160 A

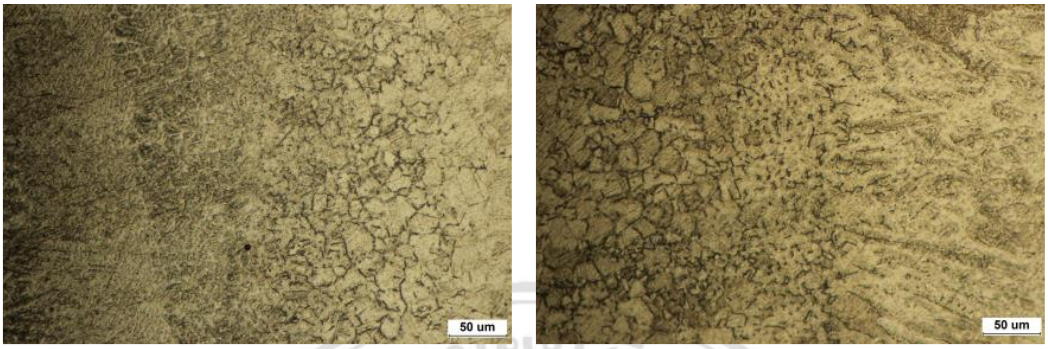

FZ → HAZ | FZ → HAZ

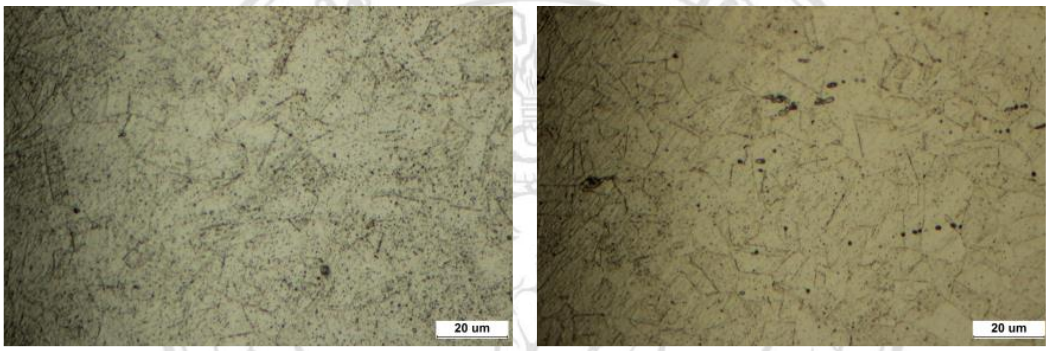

BZ mildly sensitized | BZ mildly sensitized

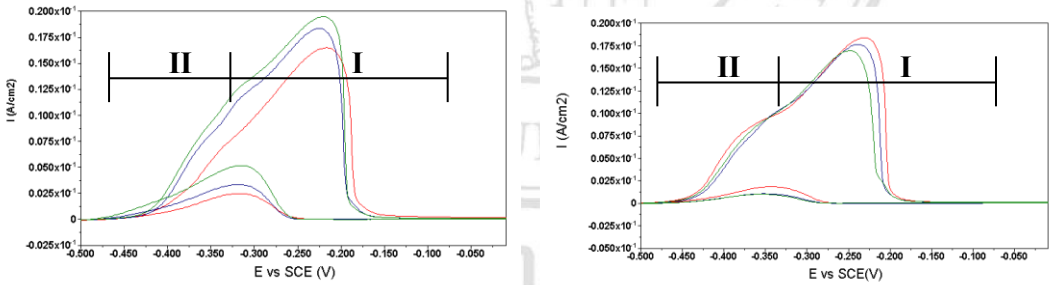

DLEPR Plots | DLEPR Plots

Mixed ratio of shield gases indicated by color as:

Red- Ar:N_2 =100: 0, Blue- Ar:N_2 = 95:5, Green- Ar: N_2 = 90:10

Figure 4.28 Grain boundary morphology of sensitized PCGTAW 201-2M and DLEPR plots at welding current 130 and 160 A under 5N_2:95 Ar

Table 4.16 DOS of PCGTAW 201-2M

Welding current (Amp)/ N_2:Ar	$I_a(\mu A/cm^2)$	$I_r(\mu A/cm^2)$	**DOS**(I_r/I_a)	**% change in DOS**
130 A				
$0N_2$:100Ar	1.748E-02	2.465E-03	1.410E-01	-63.47
$5N_2$:95Ar	1.699E-02	1.524E-03	8.976E-02	-64.48
$10N_2$:90Ar	1.639E-02	1.381E-03	8.445E-02	-65.76
160 A				
$0N_2$:100Ar	2.156E-02	7.747E-03	3.499E-01	-54.95
$5N_2$:95Ar	2.206E-02	3.424E-03	1.539E-01	-53.88
$10N_2$:90Ar	2.290E-02	4.201E-03	1.776E-01	-52.14

4.9.4 PCGTAW AISI 202

Calculated DOS values in Table 4.18 and Figure 4.29 revealed that AISI 202 base sheet and its weld specimens have severely prone to corrosion attack than other ASSs employed in the present work. Base AISI 202 had the lowest concentration of chromium and manganese. The increase in nitrogen from shielding gas was not enough to strengthen corrosion resistance as was achieved in the case of PCGTAW 201-2M. However, PCGTAW AISI 202 has some benefit as susceptibility to sensitization was less than that of the base metal as summarized in Table 4.18 and Figure 4.29.

Under Ar:N_2 = 90:10 shielding gas

Welding Current 130 A

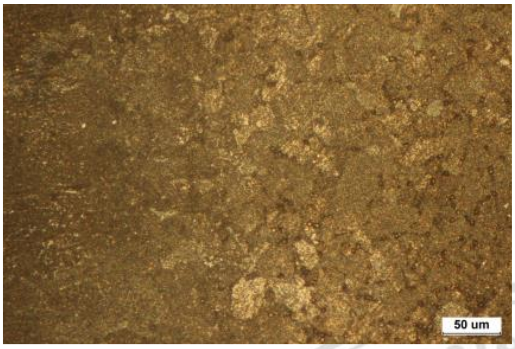

Welding Current 160 A

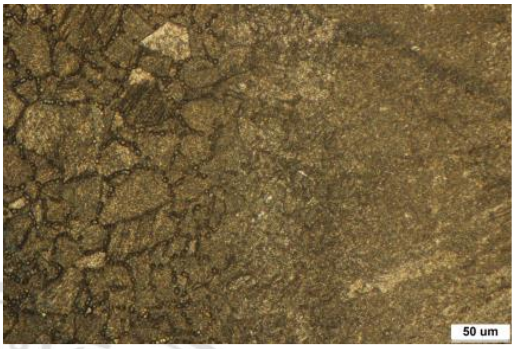

FZ → HAZ

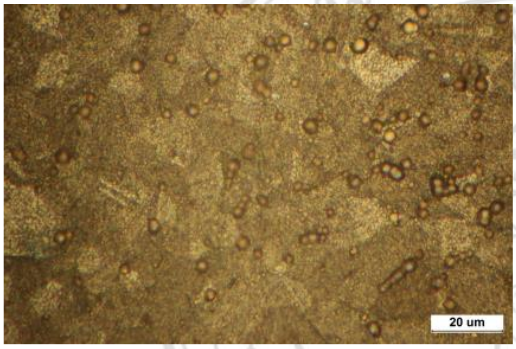

FZ → HAZ

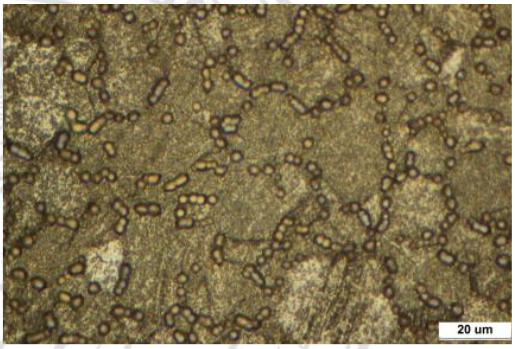

BZ mildly sensitized

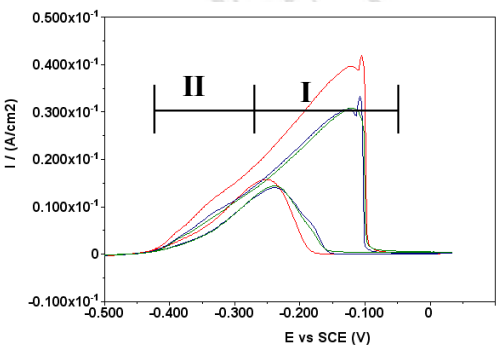

BZ mildly sensitized

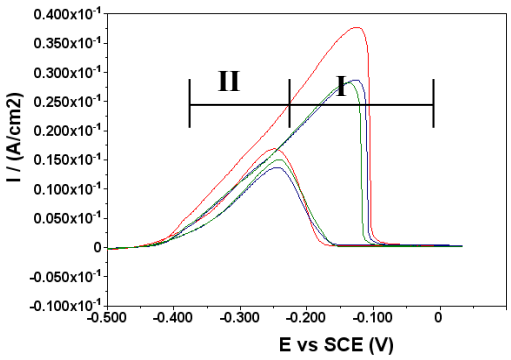

DLEPR Plots

DLEPR Plots

Mixed ratio of shield gases indicated by color as:

Red- Ar:N_2 =100: 0, Blue- Ar:N_2 = 95:5, Green- Ar: N_2 = 90:10

Figure 4.29 Grain boundary morphology of sensitized PCGTAW AISI 202 and DLEPR plots at welding current 130 and 160 A under 10N_2:90Ar

Table 4.17 DOS of PCGTAW AISI 202

Welding current (Amp)/ N_2:Ar	$I_a(\mu A/cm^2)$	$I_r(\mu A/cm^2)$	**DOS**(I_r/I_a)	**% change in DOS**
130 A				
0N_2:100Ar	4.093E-02	2.164E-02	5.299E-01	-29.55
5N_2:95Ar	4.010E-02	2.097E-02	5.224E-01	-30.98
10N_2:90Ar	3.899E-02	2.080E-02	5.334E-01	-32.90
160 A				
0N_2:100Ar	3.892E-02	1.567E-02	4.035E-01	-33.01
5N_2:95Ar	3.724E-02	1.683E-02	4.518E-01	-35.91
10N_2:90Ar	3.627E-02	1.789E-02	4.934E-01	-37.57

DOS test results obtained from PCGTAW austenitic stainless steels with controlled welding current and shielding gases can be summarized in Fig. 4.30 and as follows:

1. Optimum welding current for PCGTAW process for all austenitic stainless steel sheets employed in the present should be 130 A to maintain good corrosion properties.
2. Improvement of susceptibility to IGC had been achieved by introducing nitrogen into shielding gas around 5-10 vol.%. For the alternative 201-2M, corrosion resistance can be improved to be comparable to that of AISI 304 and AISI 304L.
3. PCGTAW AISI 202 showed the highest susceptibility to IGC. Further investigation and improvement is still needed to find the optimum controlled variables for this particular grade.

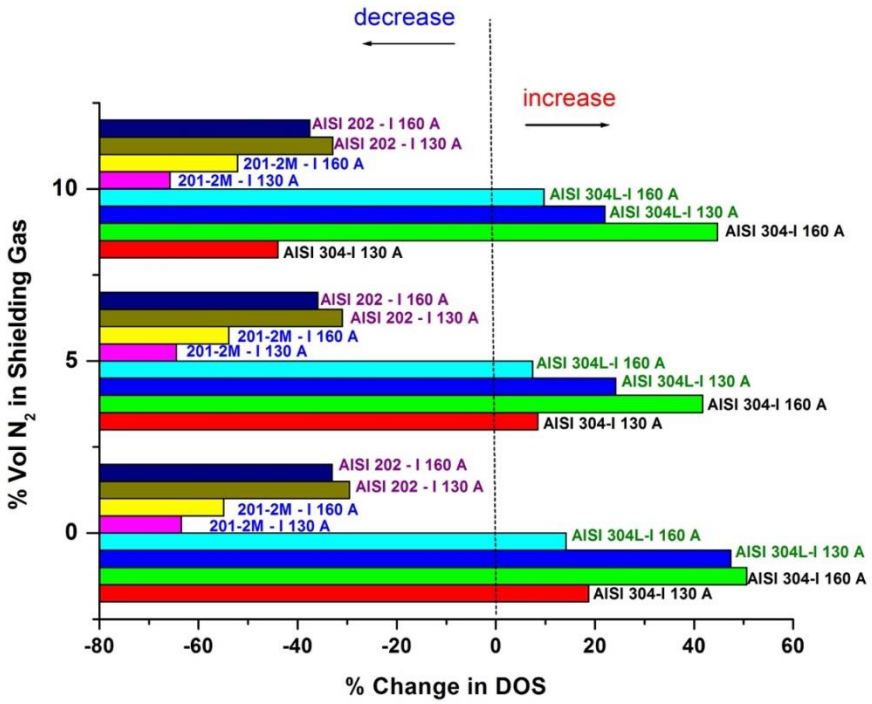

Figure 4.30 Change in DOS under different N_2 proportion in shielding gas and welding current at 130 and 160 A

4.10 Tensile Properties of Weldment

Comparison of tensile strength of PCGTAW austenitic stainless steels at welding current 130 and 160 A under 0, 5 and 10 Vol.% N_2shielding gases is given in Figure 4.31. PCGTAW 201-2M and AISI 202 under mixed shielding gas ratio of N_2:Ar = 5:95 showed the highest tensile stress. All specimens at the welding current 160 A showed a decrease in tensile stress as compared to that of their base metals. Test results of stress and strain obtained from all PCGTAW ASSs are summarized in Table C-1 and C-2 in Appendix C.

Effect of nitrogen as previously discuss in terms of austenite phase promoter had an effect on reduction of ferrite and the FN. Tensile strength of PCGTAW AISI 300s series decreased due to their FN was out of the recommended range after partially applied nitrogen into the shielding gases as well as weld integrity appeared in the distorted weld pool geometry. Nitrogen proportion in shielding gases helps to control the FN to be within range of 3 to 10 only in weld metal of PCGTAW 201-2M.

Figure 4.32 showed elongation percentage of welded specimens. Generally, the elongation percentage of PCGTAW austenitic stainless steels was increased with increasing nitrogen proportion in shielding gases.

Cross-sections of the specimens after performing tensile test were examined at the HAZ to observe the trace of hot cracking along the fracture surface as shown in Figure 4.33. PCGTAW weldment under mixed shielding gases with the ratio Ar:N_2 = 95:5 showed uniform structure of dimples and segregate particles were hardly found. Higher porosity distribution was found in PCGTAW AISI 304, AISI 304L and AISI 202 than that in the 201-2M. Despite low FNs, there was no obvious crack found in the observed areas.

The possible explanation is that nitrogen content in shielding gases had promoted austenite phase and the lower heat input from PCGTAW process itself generated rapid cooling rate that lessened the probability of detrimental phases to be formed, as mentioned earlier by Yousefieh*et al*. (2011). Therefore, reduction of hot cracking in welding of the modified high manganese 201-2M ASS can be achieved by a combination of PCGTAW process and nitrogen addition in shielding gases.

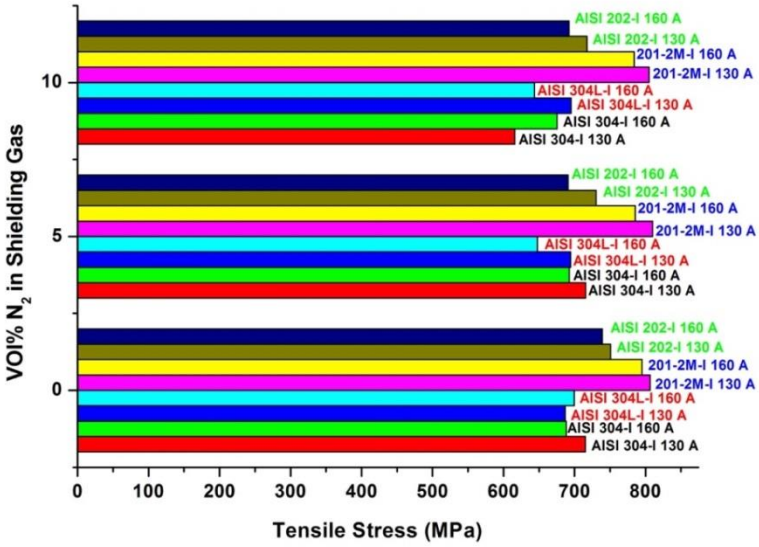

Figure 4.31 Comparison of tensile strength of PCGTAW austenitic stainless steels at welding current 130 and 160 A under 0, 5 and 10 Vol.% N_2 shielding gases

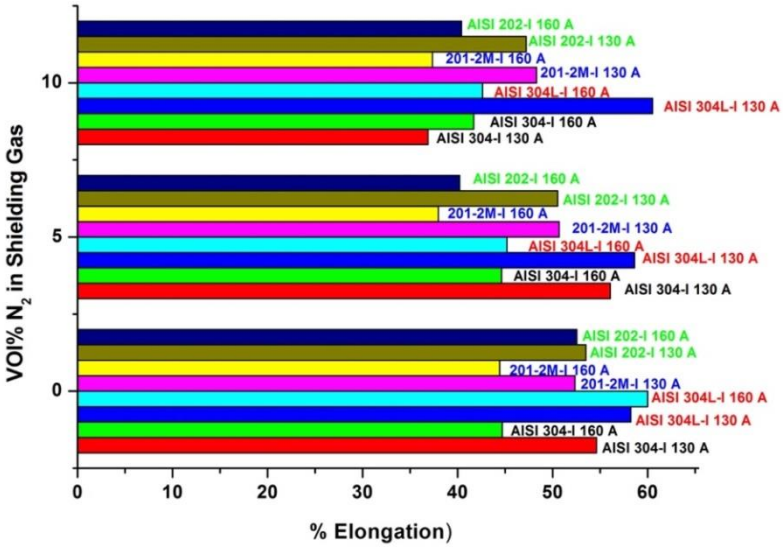

Figure 4.32 Comparison of % elongation of PCGTAW austenitic stainless steels under various Vol.% nitrogen (0, 5 and 10 %) in shielding gases.

AISI 304 **AISI 304L** **201-2M** **AISI 202**

Parent austenitic stainless steel sheets

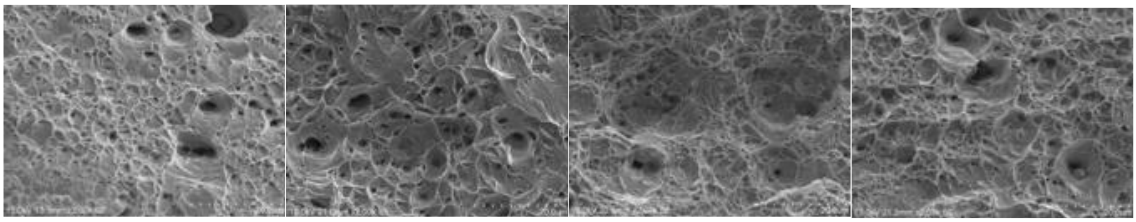

HAZ, Welding current 130 A

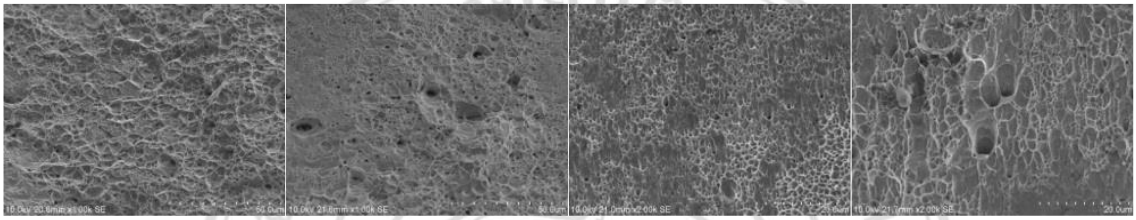

HAZ, Welding current 160 A

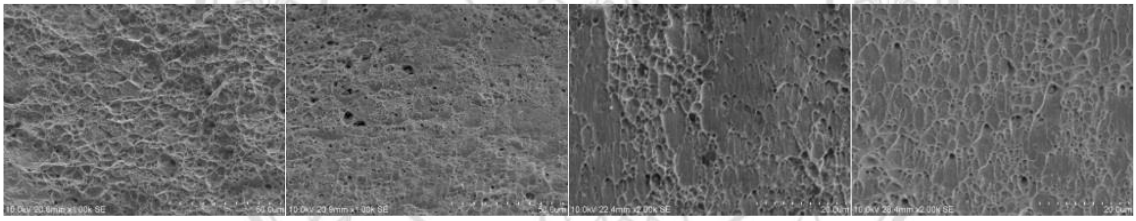

Figure 4.33 Examples of fracture surface of the base metals and PCGTAW weldment at welding current 130 and 160 A under Ar:N_2 = 95:5

4.11 Micro-Vickers Hardness of Weldment

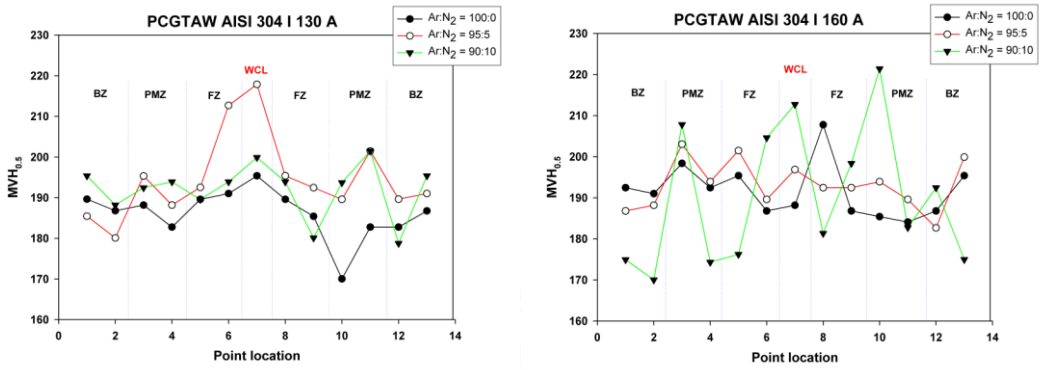

Figure 4.34 MVH of weld cross-section of PCGTAW AISI 304 at welding current 130 and 160 A.

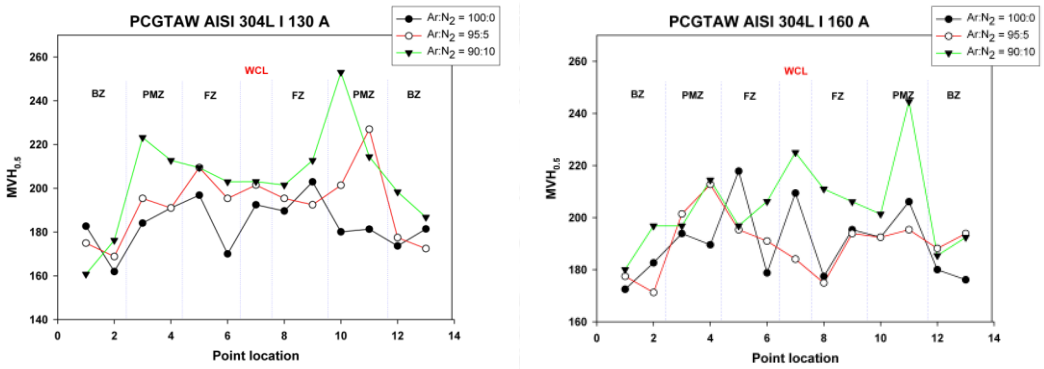

Figure 4.35 MVH of weld cross-section of PCGTAW AISI 304L at welding current 130 and 160 A.

MVH results of the PCGTAW AISI 304 and AISI 304L are given in Figs. 4.34-4.35. Comparison in terms of welding current under pure argon shielding gas, the most drastic change of MVH was showed in the partially melted zone (PMZ) and fusion zone (FZ). At nitrogen partially substitution at 5 and 10 vol% higher MVH had been found in almost every zones except base zone (BZ). It was suspected that the increase in hardness might possible occur from the precipitation of nitride compounds from nitrogen gas. It was confirmed that nitrogen addition in shielding gas at 5 vol% or higher was not appropriate for the work of PCGTAW AISI 304 and AISI 304L. However, the increase in welding current from 130 to 160 Amp help to achieve complete penetration depth but should be applied under pure argon shielding or nitrogen partially substitution less than 5 Vol%.

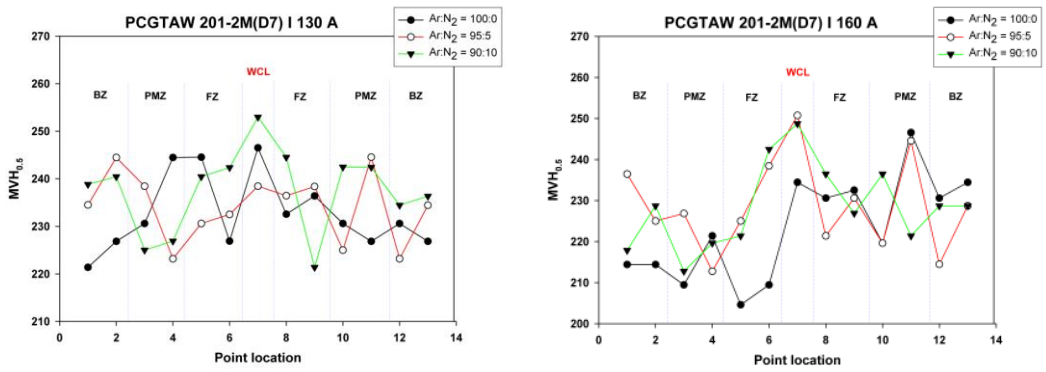

Figure 4.36 MVH of weld cross-section of PCGTAW 201-2M at welding current 130 and 160 A.

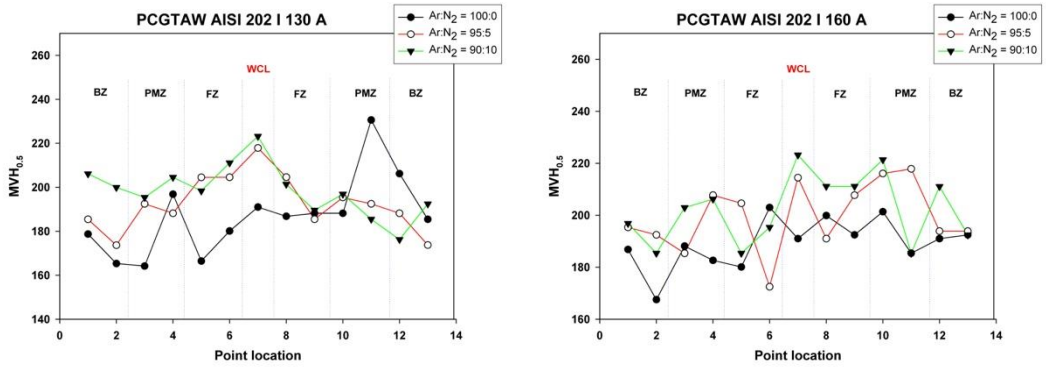

Figure 4.37 MVH of weld cross-section of PCGTAW AISI 202 at welding current 130 and 160 A.

In Figure 4.36, it was found that MVH results of PCGTAW 201-2M became more uniform in all zones at the applied welding current of 130 A under 5 Vol% nitrogen substitution when compared with the others. Moreover, the overall MVH had been reduced to close to those obtained from PCGTAW AISI 304 under pure argon shielding gas at similar welding current level. The applied welding current 130 A under 5 Vol.% nitrogen-argon mixed gases led to superior MVH and can be considered as the optimum condition for PCGTAW process of 201-2M.

MVH results of PCGTAW AISI 202 in Figure 4.37 implied that the increase in the applied welding current from 130 to 160 Amp given more uniformity in MVH distribution along both sides of weld areas from WCL. But MVH results were increase with the increase of nitrogen partially substitution in shielding gas. Therefore, the optimum applied welding current and nitrogen substitution in the PCGTAW to obtain uniform MVH should be similar to those applied with PCGTAW 201-2M.